An Explicit Simulation of Tropical Cyclones with a Triply Nested Movable Mesh Primitive Equation Model: TCM3. Part I: Model Description and Control Experiment*

YUQING WANG

International Pacific Research Center, School of Ocean and Earth Science and Technology, University of Hawaii at Manoa, Honolulu, Hawaii

(Manuscript received 2 June 2000, in final form 2 November 2000)

ABSTRACT

Results from an explicit simulation of tropical cyclones are presented in this study. The numerical model used in the study is the triply nested movable mesh primitive equation model newly developed by the author. It uses the hydrostatic primitive equations with explicit treatment of cloud microphysics. The integration domain is triply nested by a two-way nesting strategy with the two interior meshes being movable following the model tropical cyclone. The model physics are chosen based on the up-to-date developments, including an E-ϵ closure scheme for subgrid-scale vertical turbulent mixing [with E being the turbulent kinetic energy (TKE), and ϵ the TKE dissipation rate]; a modified Monin–Obukhov scheme for the surface flux calculation, with an option to include the effect of sea spray evaporation; an explicit treatment of mixed-ice phase cloud microphysics; and dissipative heating, which has been found to be important in tropical cyclones.

New developments include a new iteration scheme to solve the nonlinear balance equation in σ coordinates in the nested-mesh grids, which is used for model initialization; an initialization scheme for both TKE and its dissipation rate fields based on a level-2 turbulence closure scheme deduced from the TKE and its dissipation rate equations; and a modified formula for the timescale that determines the rate at which cloud ice converts to snow via the Bergeron process.

The success of the multiply nested movable mesh approach and the conservative property of the numerical model is first tested with an experiment in which the model was initialized with an axisymmetric cyclonic vortex embedded in a uniform easterly flow of 5 ms^{-1} on an f plane, but with no model physics. Results from a control experiment with the full model physics are then discussed in detail to demonstrate the capability of the model in simulating many aspects of the tropical cyclone, especially the inner core structure and both the inner and outer spiral rainbands in the cyclone circulation. The vortex Rossby waves in the simulated tropical cyclone core region are also identified and analyzed. Sensitivity of the model results to various model physics and major physical parameters will be given in a companion paper.

1. Introduction

The tropical cyclone is a ''localized vortex'' characterized by strong multiscale interactions. Although its horizontal extent is typically several hundred to a thousand kilometers, the energy source responsible for its formation and maintenance is the energy transferred from the ocean surface and released as latent heat in moist convective clouds within only tens of kilometers from its center. Because of the limited computational resources, in most of the earlier three-dimensional numerical models of tropical cyclones, the moist cumulus convection has been parameterized in terms of the larger-scale motions (Ooyama 1982). In this approach, the collective effect of cumulus convection is included without having cumulus convection explicitly present in the model [see Molinari and Dudeck (1992) for a review].

Despite the success of numerical models with parameterized cumulus convection in simulating many aspects of real tropical cyclones, use of implicit convection in fine-resolution models with grid spacing less than 20 km is questionable because some of the organized convection can be resolved by the model resolution and the convection is no longer a ''subgrid-scale'' phenomenon (Molinari and Dudeck 1992). Since the horizontal scale of a tropical cyclone core, as well as the rainbands in the cyclone circulation, is only tens of kilometers, simulation of the mesoscale structures and their interaction with the larger scale motions requires very high-resolution numerical models. In these models, thus, the cumulus parameterization should be bypassed and explicit simulation of convective and mesoscale motion is necessary. A complete review on this issue is given by Liu et al. (1997), who simulated both the inner core structure and the intensification of Hurricane Andrew (1992) using

*International Pacific Research Center Contribution Number IPRC-82 and School of Ocean and Earth Science and Technology Contribution Number 5359.

Corresponding author address: Dr. Yuqing Wang, IPRC/SOEST, University of Hawaii at Manoa, 2525 Correa Road, Honolulu, HI 96822.
E-mail: yqwang@soest.hawaii.edu

the Pennsylvania State University–National Center for Atmospheric Research fifth-generation, nonhydrostatic mesoscale model (MM5). The cloud physics schemes used in previous tropical cyclone models can be classified into two categories: the warm cloud processes only (e.g., Yamasaki 1977; Rosenthal 1978; Rotunno and Emanuel 1987) and the mixed/ice-phase microphysics (e.g., Willoughby et al. 1984; Lord et al. 1984; Tripoli 1992; Liu et al. 1997). The mixed/ice-phase microphysics have been shown to be responsible for generation of strong downdrafts by melting of ice particles near the melting level, and thus are very important in modeling the mesoscale structure of a tropical cyclone.

Although motions associated with the individual convective clouds are nonhydrostatic, the mesoscale motions associated with the organized cumulus convection are hydrostatic (Willoughby 1988). Both hydrostatic and nonhydrostatic models have been used with explicit cloud microphysics (e.g., Rosenthal 1978; Willoughby et al. 1984). A simulation study by Tripoli (1992) using an explicit three-dimensional nonhydrostatic mesoscale model suggests that a 10-km horizontal resolution is sufficient to approximate mature tropical cyclone dynamics, implying that nonhydrostatic effects are not crucial to storm structure and evolution. Recent studies using MM5 by D. Zhang (1999, personal communication) show that the effects of nonhydrostatic processes were not significant for the simulated Hurricane Andrew. Since in this study our emphasis will be on the mesoscale interactions in tropical cyclones, not on the individual convective cells, we will use the hydrostatic primitive equations with 5-km horizontal grid spacing and an explicit scheme for mixed/ice-phase cloud microphysics. At this resolution, subgrid-scale convection still exists and may play a significant role in tropical cyclones. Their effect can be moved downscale to the turbulent processes, which are covered by a turbulent kinetic energy (TKE) closure scheme (Detering and Etling 1985) with enhanced buoyancy production in clouds (Durran and Klemp 1982; Tripoli 1992).

Note that the initial purpose in developing the model used in this study is to provide a state-of-the-art modeling framework for advancing our strategic research on tropical cyclones. It is expected that the model can correctly represent many different physical processes, as well as the complex scale interactions that occur in real tropical cyclones. Although there are several models that are frequently used for tropical cyclone research, such as the MM5 (Grell et al. 1994; Liu et al. 1997), the movable mesh hurricane model (MMM) developed at the Geophysical Fluid Dynamics Laboratory (Kurihara et al. 1998), the model design and model physics differ from one to another, and thus the model tropical cyclones from different models can be quite different. For example, the warm core structure simulated with MMM is mostly located in the upper troposphere (around 150–250 hPa; Kurihara and Bender 1982), in agreement with observations, but that simulated with MM5 for Hurricane Andrew by Liu et al. (1997) was located in the middle troposphere (400–500 hPa). Although we do not have enough observations to justify whether the middle tropospheric warm core in the simulated Hurricane Andrew is realistic, we can see that the simulated structure may be model dependent, implying that further efforts in both development and improvement are necessary. The current effort to develop the Weather Research and Forecast model is one example (Dudhia et al. 1998).

The purpose of this paper is to describe the newly developed model, to show the success of the multiply nested movable mesh approach and the capability of the model in simulating the multiscale interactions in tropical cyclones by numerical results from control experiments. The numerical model is described in the next section together with the results from a dry experiment to show the accuracy of the numerical techniques. Parameterizations of model physics are presented in section 3. In section 4, results from a control experiment for the development of a model tropical cyclone on an f plane are discussed. Conclusions are drawn in the last section. A new initialization scheme for a tropical cyclone vortex in a σ-coordinate system with nested grids is provided in appendix B.

2. Model description

The model uses the three-dimensional hydrostatic primitive equations on either an f plane or a β plane. Using σ (pressure normalized by the surface pressure) as the vertical coordinate, the model equations are written as follows (symbols and their meanings are listed in appendix A).

Horizontal momentum equations:

$$\frac{du}{dt} = fv - \frac{\partial \Phi}{\partial x} - RT_v \frac{\partial \ln p_s}{\partial x} + F_u + D_u, \quad (1)$$

$$\frac{dv}{dt} = -fu - \frac{\partial \Phi}{\partial y} - RT_v \frac{\partial \ln p_s}{\partial y} + F_v + D_v. \quad (2)$$

Thermodynamic equation:

$$\frac{dT}{dt} = \frac{RT_v}{pC_{pm}}\omega + F_T + D_T + \frac{Q_m}{C_{pm}} + Q_R. \quad (3)$$

Surface pressure tendency equation:

$$\frac{\partial p_s}{\partial t} = -\int_0^1 \left(\frac{\partial u p_s}{\partial x} + \frac{\partial v p_s}{\partial y}\right) d\sigma. \quad (4)$$

Vertical σ-velocity:

$$\dot{\sigma} = -\frac{1}{p_s}\left[\sigma \frac{\partial p_s}{\partial t} + \int_0^\sigma \left(\frac{\partial u p_s}{\partial x} + \frac{\partial v p_s}{\partial y}\right) d\sigma\right]. \quad (5)$$

Hydrostatic relation:

$$\frac{\partial \Phi}{\partial \ln \sigma} = -RT_v\left(1 + \frac{q_c + q_r + q_i + q_s + q_g}{1 + q_v}\right)^{-1}. \quad (6)$$

Equation for mixing ratio of water vapor (q_v):

$$\frac{dq_v}{dt} = S_v + F_q + D_q. \tag{7}$$

Equation for mixing ratios of liquid (solid) water substances:

$$\frac{dq_x}{dt} = S_x + D_{q_x}. \tag{8}$$

where q_x can be cloud water (q_c), rainwater (q_r), cloud ice (q_i), snow (q_s), or graupel (q_g).

Equations for turbulence kinetic energy (E) and its dissipation rate:

$$\frac{dE}{dt} = S_E + F_E + D_E, \tag{9}$$

$$\frac{d\varepsilon}{dt} = S_\varepsilon + F_\varepsilon + D_\varepsilon. \tag{10}$$

In the above equations

$$\frac{d}{dt} = \frac{\partial}{\partial t} + u\frac{\partial}{\partial x} + v\frac{\partial}{\partial y} + \dot{\sigma}\frac{\partial}{\partial \sigma}. \tag{11}$$

The boundary conditions of $\dot{\sigma} = 0$ at $\sigma = 0$ and 1 are implied in (4) and (5). Terms of F_x and D_x are vertical and horizontal diffusions, respectively. In order to conserve the total energy of the adiabatic system, the ω term in the thermodynamic equation (3) is given by

$$\frac{RT_v\omega}{pC_{pm}} = \frac{R}{C_{pm}}\left[T_v\left(\frac{1}{p_s}\frac{\partial p_s}{\partial t} + \dot{\sigma}\frac{\partial \ln\sigma}{\partial \sigma}\right) + \left(uT_v\frac{\partial \ln p_s}{\partial x} + vT_v\frac{\partial \ln p_s}{\partial y}\right)\right]. \tag{12}$$

The specific heat for moist air C_{pm} in (3) is given by

$$C_{pm} = C_p(1 + 0.81q_v). \tag{13}$$

The governing equations are discretized using the second-order conservative finite-difference scheme [Lilly (1964) on an unstaggered grid system (the Arakawa A grid)]. The time integration is accomplished using the second-order leapfrog scheme with intermittent use of the Euler-backward scheme to suppress the high-frequency numerical noise. Each large time step (Δt) of integration consists of one small time step ($\delta t = \Delta t/N$, $N = 6$ in the current model) of the Euler-backward scheme followed by $N - 1$ small time steps of the leapfrog scheme with the standard time filtering (with a filtering coefficient of 0.05) to damp computational modes for the adiabatic component of the model. A physical process stage is performed at the end of the dynamical component, with a time step of Δt. In order to prevent a false cascade of energy to grid-scale structure through nonlinear aliasing due to the use of the unstaggered grid, the horizontal diffusion terms are included in the adiabatic stage and integrated with small time steps.

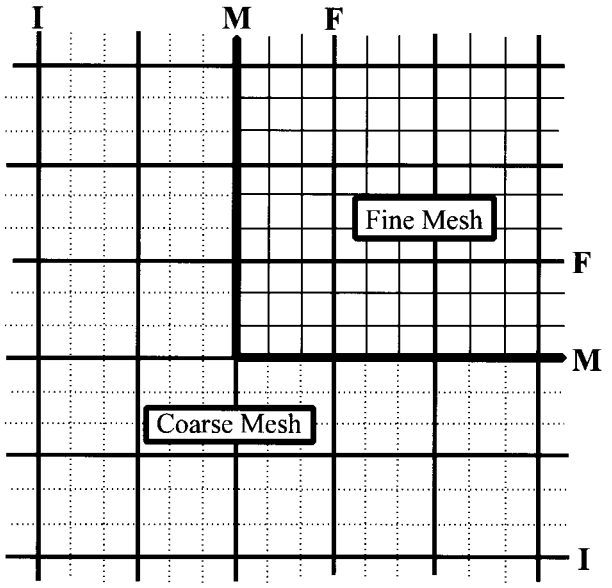

FIG. 1. The interface structure, showing the separation of the input interface (I) and the feedback interface (F) from the mesh interface (M).

The model atmosphere is divided vertically into 20 layers from $\sigma = 0$ to $\sigma = 1$, with the interfaces $\sigma =$ 0.04, 0.07, 0.09, 0.11, 0.14, 0.17, 0.21, 0.27, 0.35, 0.45, 0.55, 0.65, 0.74, 0.82, 0.88, 0.93, 0.96, 0.984, 0.994. Horizontal velocity, temperature, geopotential, and all moisture variables are defined in the middle of each layer, but the vertical σ velocity, prognostic turbulence variables, and vertical turbulent fluxes are carried at the interfaces. For upper and lower boundary conditions, we require that fluid particles do not cross the $\sigma = 0$ and $\sigma = 1$ surfaces, and that there are no vertical turbulent fluxes at the top of the model atmosphere. The model domain is triply nested in the horizontal. The ratios of grid length and time step of the three meshes are 9:3:1, respectively. The outermost mesh domain is fixed with a cyclic boundary condition in the zonal direction and an open boundary condition for the north and south boundaries. Positioning of the two internal mesh domains is determined with respect to the location of the model tropical cyclone so that each mesh center is always within one grid distance from the model cyclone center. The mesh movement during the time integration is treated by the same algorithm as used by Kurihara and Bender (1980). The fields on the leading side of the fine mesh are obtained by cubic spline interpolation with positive-definite constraints for all moisture and turbulence variables.

The two-way interactive nesting strategy is adopted in the model. As suggested by Zhang et al. (1986), in order to reduce the numerical noise near the mesh interfaces, two dynamic interfaces between neighboring meshes are defined: the input interface (I in Fig. 1) at which the coarse mesh provides the boundary values

for the fine mesh; and the feedback interface (F in Fig. 1) at which the predicted fine mesh values are used to update the coarse mesh fields. The input interface is outside the mesh interface by two grid points of coarse mesh, and the feedback interface is one grid point of coarse mesh inward from the mesh interface M (Fig. 1). In this two-way nesting system, time integration proceeds in the following way. First, the prediction with a coarse time step is performed for the coarse mesh. Then the prediction for the fine mesh domain proceeds with the fine time step until the time level of the fine mesh aligns with that of the coarse mesh. The conditions at the boundary (line I) for the fine mesh domain at each fine time step are derived successively by both time and space interpolation from the prediction of the coarse mesh using a linear time interpolation and a cubic spline spatial interpolation with positive-definite constraints for all moisture and turbulence variables. Note that due to the influence of finite differencing and multi–time steps for the dynamical component, the fine mesh prediction is valid only within the mesh interface M.

Feedback from the fine mesh fields to the coarse mesh occurs when the time level of the fine mesh integration matches that of the coarse mesh integration. At this time, fields at the grid points of the coarse mesh in the interior of the fine mesh are updated by the prediction from the fine mesh domain, using the nine-point average suggested by Zhang et al. (1986):

$$F_{I,J} = f_{i,j} + \frac{\xi(1-\xi)}{2}(f_{i-1,j} + f_{i,j-1} + f_{i+1,j} + f_{i,j+1} - 4f_{i,j}) + \frac{\xi^2}{4}(f_{i-1,j-1} + f_{i+1,j-1} + f_{i-1,j+1} + f_{i+1,j+1} - 4f_{i,j}), \quad (14)$$

where ξ is the smoothing coefficient (0.5), F denotes the value of any prognostic variables at grid points of coarse mesh, f represents their values at the fine grid points predicted by the fine mesh, and the subscripts I, J define the same grid point in coarse mesh as i, j in the fine mesh. Note that the feedback is only performed in the interior domain of the fine mesh.

To reduce the difference across the mesh interface due to different truncation errors in the two adjacent meshes, the final predicted fields in the narrow zone between M and F are further weighted using predictions from both the fine and coarse meshes, that is, for any prognostic variable F, we have

$$F = w(n)F_f + [1 - w(n)]F_c, \quad (15)$$

where F_f and F_c are predictions from the fine and coarse meshes, respectively, and n the grid index inward from the mesh interface M; $w(n)$ is a weighting function taken to be 0.0, 0.2, 0.6, 0.9 for the outermost four grid points, and 1.0 for all other interior grid points. The noise near the lateral boundaries associated with either mesh nesting or mesh movement is suppressed by a five-point smoothing operator defined as

$$\overline{F_n} = (1 - 4S_n)F_n + S_n \sum (F, \overline{F})_{i,j}, \quad n = 1, 2, \ldots, N_b, \quad (16)$$

where subscript n denotes the gridpoint index inward from and normal to the lateral boundaries. The quantities with overbars are smoothed values, $\sum(F, \overline{F})_{i,j}$ is the sum of F or $\overline{F}$ at four grid points at a distance of $\sqrt{2}$ grid spacing from grid point (i, j) and N_b is the total number of grid points being smoothed. The smoothing coefficient S_n takes the following form:

$$S_n = 0.125(N_b - n + 1)/N_b. \quad (17)$$

The smoothing is carried out for u, v, T, and q_v, and p_s from the first interior grid inward over $N_b = 5$ grid points for the internal meshes, and 20 for the north and south boundaries for the outermost mesh.

Since the finite difference on the unstaggered A grid usually suffers from grid-scale noise, horizontal filtering is necessary to prevent the false cascade of energy to structures near the grid scale, and the solution separation (Purser and Leslie 1988). Horizontal diffusion can only partially damp the amplitudes of small-scale components generated by the finite-difference scheme. Therefore, a horizontal smoothing-desmoothing operation (Grell et al. 1994) is used for u, v, T, and p_s fields at every six time steps, with smoothing and desmoothing coefficients of 0.5 and -0.51 in (14). This smoothing-desmoothing operation removes noise with two-grid-point waves completely but preserves waves with the wavelength greater than three grid points well (Bender et al. 1993; Kurihara et al. 1998). Note that the desmoothing coefficient is increased with σ^2 between $\sigma = 0.16$ and $\sigma = 0.08$ from -0.51 to 0.0 and is kept at 0.0 when $\sigma \leq 0.08$. Such a reduction of desmoothing in the upper troposphere and the stratosphere is used for minimizing the reflection of upward propagating gravity waves generated by deep convection. To reduce the reflection of outward propagating gravity waves near the lateral boundaries, the desmoothing coefficient is also reduced by weighting of 0.0, 0.0, 0.3, 0.7, 0.9 for the second, third, fourth, fifth, and sixth grid points inward from the lateral boundaries in each mesh. We found that these procedures are very effective for removing grid-scale noise, and are adequate to prevent solution separation associated with the unstaggered grid system.

To test the success of the multiply nested movable mesh approach, and the conservative property of the model, an experiment with no model physics was performed. The model was initialized with an axisymmetric cyclonic vortex embedded in a uniform easterly flow of 5 m s^{-1} on an f plane (18°S). The initially axisymmetric cyclonic vortex has a deep cyclonic circulation throughout the troposphere, whose tangential flow is defined by

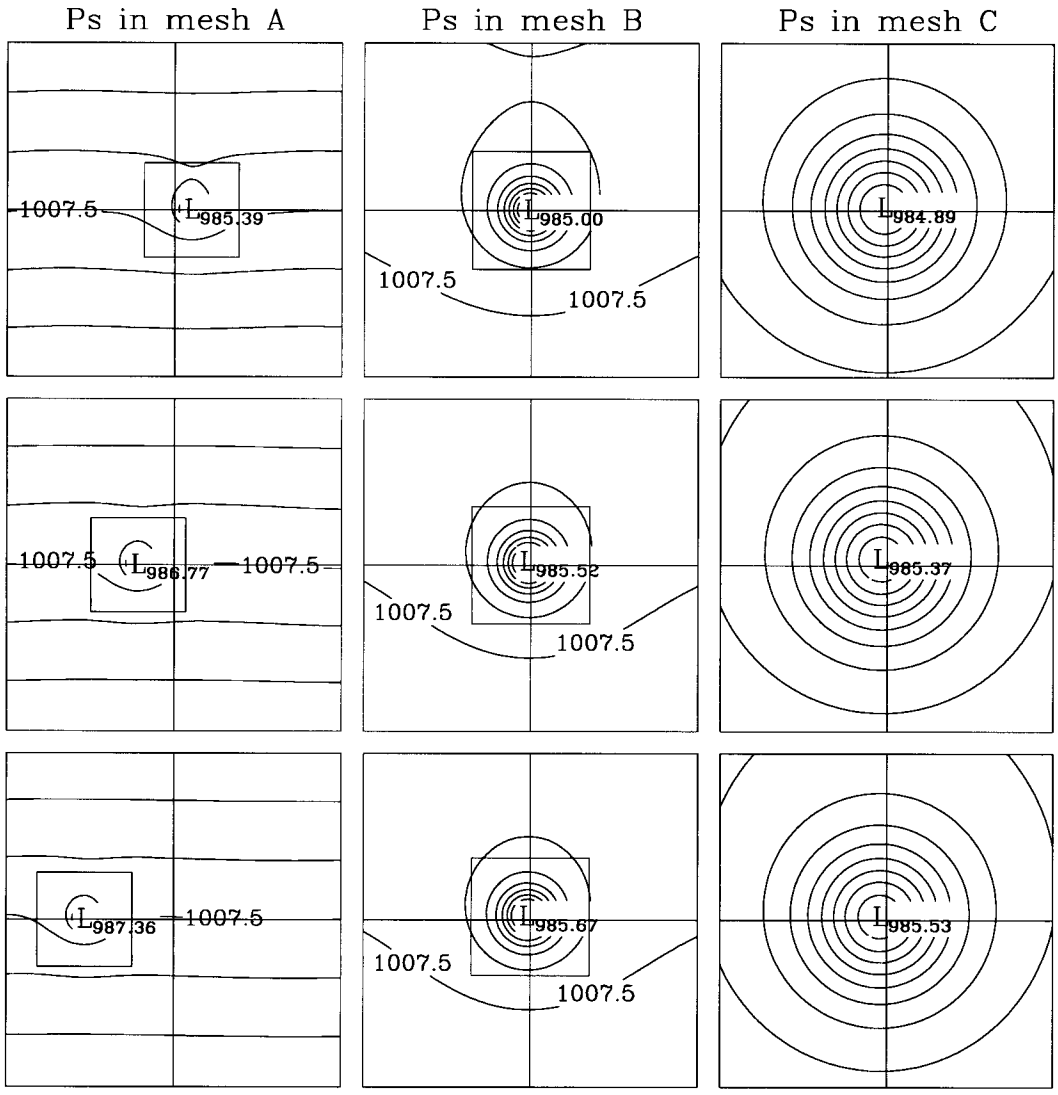

FIG. 2. Surface pressure fields in the three mesh domains in the experiment with no model physics after (top) 48 h, (middle) 96 h, and (bottom) 144 h of time integration. Only a domain of 121 by 121 grid points in mesh A is shown.

$$V_T(r, \sigma) = \begin{cases} \dfrac{3\sqrt{6}}{4} V_m \left(\dfrac{r}{r_m}\right)\left[1 + \dfrac{1}{2}\left(\dfrac{r}{r_m}\right)^2\right]^{-3/2} \sin\left[\dfrac{\pi}{2}\left(\dfrac{\sigma - \sigma_u}{1 - \sigma_u}\right)\right], \\ \qquad\qquad \sigma > \sigma_u; \\ 0.0, \qquad \sigma \le \sigma_u; \end{cases} \tag{18}$$

where r denotes radial distance from the vortex center, V_m the maximum tangential wind at the radius of r_m, and $\sigma_u = 0.1$. The initial vortex has a maximum azimuthal wind of 30 m s^{-1} at a radius of 100 km. The initial relative humidity and the environmental sounding are assumed horizontally homogeneous and have vertical profiles of the monthly mean of January at Willis Island, northeast of Australia (Holland 1997), which is representative of tropical ocean conditions. The sea surface temperature is fixed at 29°C. The resolutions for the three meshes are 45, 15, and 5 km, respectively, with corresponding time steps Δt of 450, 150, and 50 s. The three domains consist of 141 by 121, 103 by 103, and 109 by 109 grid points, respectively. The model was run for 168 h.

Figure 2 shows the sea surface pressure fields in the three mesh domains in this experiment after 48 h (top), 96 h (middle), and 144 h (bottom) of time integration. It can be seen that there is no observable noise in the mesh interfaces and the isobars cross the mesh interface smoothly. This demonstrates that noise is minimal and is successfully controlled in our two-way nesting, movable mesh system. The intensity of the vortex was well maintained in the model since there were no model physics included in this experiment. This indicates that

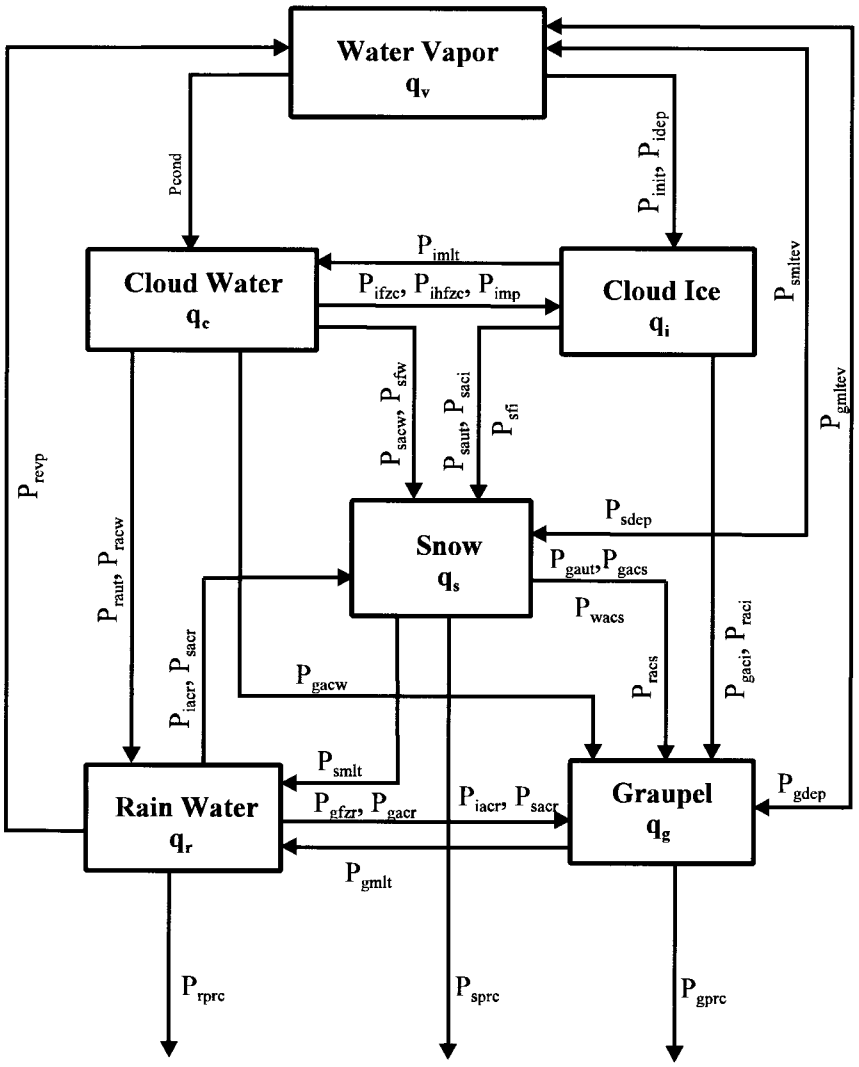

FIG. 3. The cloud microphysical processes considered in the model. See appendix B and Table 1 for an explanation.

there is neither significant sources nor sinks from our numerical scheme. We found that the high resolution and the conservative numerical scheme used in the model are both important.

3. Model physics

a. Cloud microphysics parameterization

The parameterization of cloud microphysics is based on the existing schemes that have been extensively tested and used in cloud-/mesoscale models in recent years (e.g., Lin et al. 1983; Rutledge and Hobbs 1983, 1984; Ikawa and Saito 1991; Reisner et al. 1998). The major effort has been to modify some tuning parameters to be more relevant to tropical convection or tropical cyclones (McCumber et al. 1991). The mixing ratios of cloud water, rainwater, cloud ice, snow, and graupel are all prognostic variables in the model. Cloud water is assumed to be monodispersed and to move with the air, while cloud ice is monodispersed but precipitates with the terminal velocity given by Heymsfield and Donner (1990). Condensation/evaporation of cloud water takes place instantaneously when the air is supersaturated/subsaturated.

The microphysical processes considered in the model are summarized in Fig. 3 and the acronyms are explained in Table 1. Description and their parameterization of these processes can be found in the references given in Table 1 and also in detail in Wang (1999). There have been several modifications since Wang (1999). In the current version, the number concentration of primary ice nuclei and the intercept parameter for graupel are modified according to the latest release of MM5V3.3 (REISNER2). A modification to the original formula for the timescale, which determines the rate at which cloud

TABLE 1. Acronyms for model microphysical processes.

Acronym	Meaning and references
P_{cond}	Condensation of water vapor (Reisner et al. 1998)
P_{gaci}	Collection of cloud ice by graupel (Rutledge and Hobbs 1984)
P_{gacr}	Collection of rain by graupel (Lin et al. 1983)
P_{gacs}	Collection of snow by graupel (Lin et al. 1983)
P_{gacw}	Collection of cloud water by graupel (Rutledge and Hobbs 1984)
P_{gaut}	Snow crystal aggregation to form graupel (Lin et al. 1983)
P_{gdep}	Depositional growth of graupel (Rutledge and Hobbs 1984)
P_{gfzr}	Freezing of rain to form graupel (Bigg 1953)
P_{gmlt}	Melting of graupel (Rutledge and Hobbs 1984)
P_{gmltev}	Evaporation of melting graupel (Rutledge and Hobbs 1984)
P_{gprc}	Sedimentation of graupel
P_{iacr}	Collection of rain by cloud ice (Rutledge and Hobbs 1984)
P_{idep}	Depositional growth of cloud ice (Ikawa and Saito 1991)
P_{ifzc}	Freezing cloud water to form cloud ice (Ikawa and Saito 1991)
P_{ihfzc}	Homogeneous freezing of cloud water (Reisner et al. 1998)
P_{imlt}	Immediate melting of cloud ice in region $T > 0$°C (Reisner et al. 1998)
P_{imp}	Ice multiplication growth (Hallett and Mossop 1974)
P_{init}	Initiation of cloud ice (Grell et al. 1994)
P_{iprc}	Sedimentation of cloud ice
P_{raut}	Autoconversion of cloud water to form rain (Kessler 1969)
P_{raci}	Collection of cloud ice by rain (Lin et al. 1983)
P_{racs}	Collection of snow by rain (Lin et al. 1983)
P_{racw}	Collection of cloud water by rain (Grell et al. 1994)
P_{revp}	Evaporation of rain (Orville and Kopp 1977)
P_{rprc}	Precipitation of rain
P_{saci}	Collection of cloud ice by snow (Rutledge and Hobbs 1984)
P_{sacr}	Collection of rain by snow (Lin et al. 1983)
P_{sacw}	Collection of cloud water by snow (Rutledge and Hobbs 1984)
P_{saut}	Autoconversion of cloud ice to form snow (Rutledge and Hobbs 1984)
P_{sdep}	Depositional growth of snow (Rutledge and Hobbs 1984)
P_{sfi}	Snow growth from cloud ice via Bergeron process (Koenig 1971, modified)
P_{sfw}	Snow growth from cloud water via Bergeron process (Hsie et al. 1980, modified)
P_{smlt}	Melting of snow (Lin et al. 1983)
P_{smltev}	Evaporation of melting snow (Rutledge and Hobbs 1984)
P_{sprc}	Sedimentation of snow
P_{wacs}	Loss of snow due to collision with cloud water (Rutledge and Hobbs 1984)

ice converts to snow via the growth of Bergeron process embryos, has been made to account for the effect of ice supersaturation and the difference between the saturation mixing ratios on water and ice surfaces. The modified formula predicts a relatively short timescale in regions with cloud water, and a substantially larger timescale in the anvil clouds, outside the region with cloud water. This modification is more physically reasonable than the approach proposed by Krueger et al. (1995) and is summarized in appendix C. Time integration of the precipitation (sedimentation) of cloud ice, rain, snow, and graupel is carried out by a first-order implicit upwinding scheme.

b. Subgrid-scale horizontal diffusion

The subgrid-scale horizontal diffusion is calculated with a second-order form ($K_H\nabla^2 X$), with the horizontal eddy diffusion coefficients K_H defined by

$$K_H = \eta\left(K_{\rm H0} + \frac{1}{2}k^2d^2|D|\right), \qquad (19)$$

where d is the grid spacing; k the von Kármán constant (0.4); η a constant of 1.0 for D_u, D_v, D_T, 0.5 for D_q, and 0.0 for D_E, D_ϵ, and all the hydrometeors (D_{qx}). Here $K_{\rm H0}$ is a background diffusion coefficient which is a function of grid spacing, $K_{\rm H0} = \gamma d$ with $\gamma = 0.4$ for the internal mesh domains and $\gamma = 0.6$ for the outermost mesh domain. The deformation of the horizontal wind is $|D|$.

In order to suppress reflection of outward propagating gravity waves at the lateral boundary of each mesh, the actual lateral diffusion coefficient K_H in (19) is increased in a narrow zone around the lateral boundary by a factor of φ, which is defined as

$$\varphi = N_b - n + 1, \qquad n = 1, 2, 3, \ldots, N_b, \qquad (20)$$

where n is the gridpoint index inward from the lateral boundary, and N_b is the total number of grid points in the narrow zone around the boundary. We simply set $N_b = 5$ for the internal meshes, and 20 for the north and south boundaries in the outermost mesh.

c. Turbulent fluxes at the sea surface

The direct turbulent fluxes of momentum, heat, and moisture at the sea surface are calculated based on the

Monin-Obukhov similarity theory with some modifications to the stability functions for momentum, heat, and moisture in highly unstable conditions used by Fairall et al. (1996). The roughness length for momentum z_u over the ocean is calculated according to the Charnock relationship with the Charnock constant of 0.016 (Garratt 1992) and with an additional term added to account for the effect of molecular kinematic viscosity as suggested by Wu (1982). It can be written as

$$z_u = 0.016\frac{u_*^2}{g} + 0.11\frac{\mu}{u_*}, \tag{21}$$

where μ is the dynamic viscosity of air and u_* the friction velocity. The roughness lengths for heat and moisture, however, are assumed to be constant and given by

$$\begin{cases} z_T = \max(4.9 \times 10^{-5},\ 0.2\mu/u_*) \\ z_q = \max(1.3 \times 10^{-4},\ 0.3\mu/u_*). \end{cases} \tag{22}$$

The constants used in (22) are based on Large and Pond (1982). A lower bound for either z_T or z_q is assumed so that the roughness length is not allowed to be less than the value corresponding to a smooth surface (Garratt 1992). The drag coefficient and the exchange coefficients for heat and moisture are then obtained by an iteration scheme similar to that used by Fairall et al. (1996).

The bulk parameterization scheme for sea spray evaporation proposed by Fairall et al. (1994) is included as an option to consider the effect of sea spray evaporation on surface heat and moisture fluxes. Two critical assumptions made in this parameterization scheme are: 1) spray droplets are injected at the wave height and 2) the droplets adjust rapidly to the wet-bulb temperature, but fall back into the sea before they have lost a large proportion of their mass. With the effect of sea spray evaporation, the total surface heat and moisture fluxes become

$$\begin{aligned} &\text{Heat flux:} && H + Q_s - Q_l. \\ &\text{Moisture flux:} && E_v + Q_l/L_v, \end{aligned} \tag{23}$$

where H and E_v are the direct heat and moisture fluxes; Q_s and Q_l are the sensible and latent heat fluxes, respectively, due to sea spray; and L_v the latent heat of condensation.

Note that the parameterization given by Fairall et al. (1994) is valid for wind speeds up to 30 m s^{-1} but can be reasonable for wind speeds up to 40 m s^{-1} (Fairall et al. 1994). However, we expect that when the wind speeds are over 40 m s^{-1} the lowest part of the atmosphere is nearly saturated due to evaporation from both the ocean surface and precipitating rain. In this case, even though the same parameterization scheme is used, contribution from the sea spray evaporation will be small (Wang et al. 1999).

d. Subgrid-scale vertical diffusion

The subgrid-scale vertical diffusion is accomplished by a 1.5-order turbulence closure scheme (the so-called E-ϵ closure scheme), in which both the TKE and its dissipation rate are prognostic variables (Detering and Etling 1985). Our implementation of this parameterization scheme is similar to the one used by Langland and Liou (1996) except that a modification is made to the calculation of the buoyancy production term so that the moist-adiabatic processes in cloudy air are taken into account (Durran and Klemp 1982; Tripoli 1992).

As in Langland and Liou (1996), to avoid large time truncation errors, a short time step (the same as that used in the finest mesh) in the two coarser meshes was used in the model. In order to reduce the spinup time for the turbulence fields during the model time integration, we proposed using the level-2 turbulent closure scheme deduced from the full TKE and its dissipation rate equations to initialize both TKE and its dissipation rate fields (see Wang 1999 for a detail). We first update the turbulence fields and then the updated new turbulence fields are used to evaluate the vertical diffusion coefficients for momentum, heat, and moisture. Time integration of the vertical diffusion coupled with the surface layer is then carried out by an implicit scheme.

e. Radiational heating/cooling

The effect of radiative transfer is not treated explicitly in the current version of the model. Instead, a Newtonian cooling is added in the thermodynamic equation, as used in the tropical cyclone model of Rotunno and Emanuel (1987):

$$Q_R = -\frac{\theta - \theta_{\text{ref}}}{\tau_R}, \tag{24}$$

where θ_{ref} is the reference potential temperature profile of the undisturbed mean tropical environment. Here τ_R is a relaxation timescale for radiative cooling and is taken to be 24 h. In order to remove the unrealistically large cooling in the cyclone core region, we enforce $|Q_R| < 2$ K day^{-1}, which is equivalent to the radiative cooling in the tropical atmosphere (Anthes 1982).

f. Dissipative heating

The effect of dissipative heating has traditionally been neglected in either numerical models or theoretical studies of tropical cyclones. Recently, Bister and Emanuel (1998) examined its effect on the maximum potential intensity of tropical cyclones both theoretically and numerically. They found that inclusion of dissipative heating increases the maximum intensity of tropical cyclones by about 25% in maximum wind speeds and 40% in central pressure deficit in their tropical cyclone model. More recently, Zhang and Altshuler (1999) further examined the effect of dissipative heating on tropical

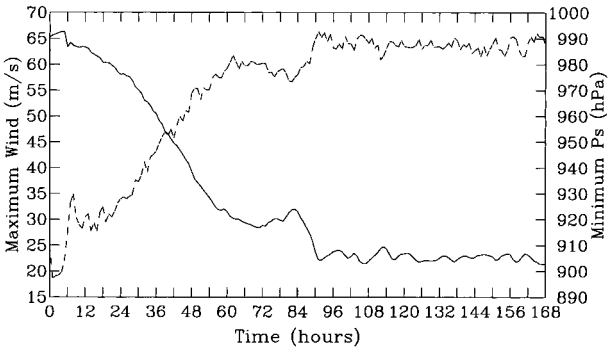

FIG. 4. The (a) minimum sea surface pressure and (b) maximum wind at the lowest model level as a function of time in the control experiment for the development of a tropical cyclone on an f plane in an environment at rest (solid) together with results for the corresponding dry vortex shown in Fig. 2 (dashed).

cyclone intensity using a 72-h explicit simulation of Hurricane Andrew with MM5. They found that inclusion of dissipative heating increases the central pressure deficit by 5–7 hPa and maximum surface wind by about 10%. They also showed that dissipative heating tends to warm the surface layer, leading to a decrease in sensible heat flux at the sea surface, with a net heating rate being 30%–40% greater than the simulation without dissipative heating included.

The idea of dissipative heating is that friction dissipates the kinetic energy by molecular motion, which increases the thermal energy. In our model, this effect is simply expressed as

$$C_p \left.\frac{\partial T}{\partial t}\right|_{\text{dis}} = -\left.\frac{\partial K}{\partial t}\right|_{\text{dis}} = -(uF_u + vF_v), \qquad (25)$$

where K is the kinetic energy.

4. Control experiment

In this section, results from a control experiment are discussed. The experiment is designed to demonstrate the capability of the model in simulating the development and structure of the tropical cyclone. The model is initialized with the same vortex as that used in section 2 but with an initial maximum tangential wind of 25 m s^{-1}, in an environment at rest, and all model physics included except for the effects of sea spray and dissipative heating, which will be included in our sensitivity experiments in Part II.

The evolution of the minimum sea surface pressure and the maximum wind speed at the lowest model level over 168-h integration is shown in Fig. 4. After an initial drop in maximum wind due to the lack of a boundary layer of the initial vortex, a rapid intensification occurred up to 54 h, followed by a slowly varying stage during which the cyclone weakened from 72 h to 84 h, and then by a reintensification between 84 and 90 h. This was followed by a quasi-steady stage during which

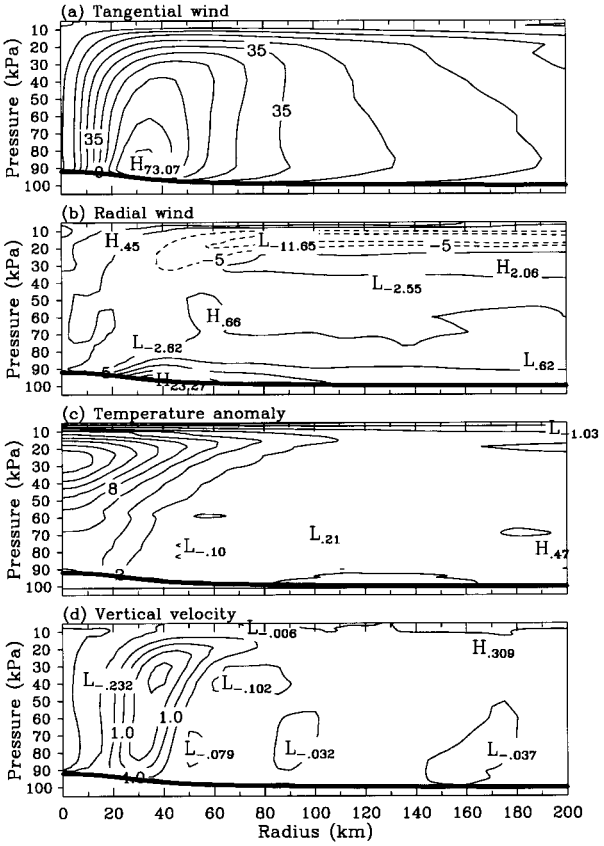

FIG. 5. Height-radius distribution of the azimuthal mean of (a) tangential and (b) radial flow, (c) temperature anomalies from the undisturbed environment, and (d) vertical velocity after 60 h of time integration in the control experiment. Units are m s^{-1} in (a), (b), (d), K in (c). Solid line shows the azimuthal mean surface pressure.

the cyclone intensity oscillated slightly with time. The cyclone reached a maximum intensity of 66.2 m s^{-1} in maximum wind (occurred at about 91 h) and a minimum central surface pressure of 903 hPa (occurred at about 107 h).

The vertical–radial structure of the azimuthal mean tropical cyclone after 66 h of time integration is shown in Fig. 5. The maximum tangential wind is at about 30-km radius, and tilts outward with height (Fig. 5a). Strong inflow occurs in the boundary layer below about 800 hPa (Fig. 5b) with maximum inflow of about 23 m s^{-1} at about 40 km from the cyclone center, just outside the radius of maximum tangential wind. A broad outflow layer is located in the upper troposphere outside the eyewall with its roots at lower levels in the eyewall. The model cyclone has a warm core structure with a maximum temperature anomaly of 16°C between 250 and 300 hPa (Fig. 5c). The upper-level warming extends to large radii. The relatively cold area below about 600 hPa is a result of melting of snow and graupel in the stratiform precipitation region. There is a weak descending motion in the eye and strong updraft in the eyewall, which tilts outward with height as well (Fig. 5d). Note

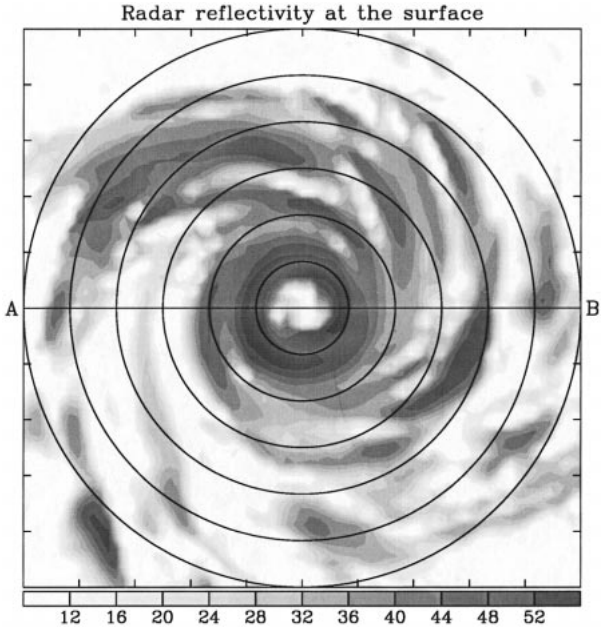

FIG. 6. A plan view of the modeled radar reflectivity (unit: dBZ) at the sea surface after 60 h of time integration in the control experiment. The domain shown is 360 km by 360 km with circles of every 30 km from the cyclone center.

that the maximum descending motion in the eye occurs near the inner edge of the eyewall, which is originated from the returning flow at the top of the eyewall (Fig. 5b) and is enhanced by the sublimative cooling of ice-phase hydrometeors detrained from the eyewall. All these features are comparable with the observations of real tropical cyclones (Frank 1977), and some other simulations (e.g., Liu et al. 1997, 1999).

A plan view of the modeled radar reflectivity (calculated by the same algorithm as in Liu et al. 1997) at the surface after 66 h of time integration is given in Fig. 6, which shows the existence of an eye with a polygonal shape, an eyewall with high reflectivity, and both inner and outer rainbands. We have found that quite different mechanisms are responsible for formation and evolution of inner and outer rainbands. The inner rainbands formed as a result of interaction that occurred between the vortex Rossby waves in the core and the eyewall convection, as expected by Montgomery and Kallenbach (1997), while the outer rainbands were initiated by downdrafts in the stratiform cloud region and maintained like squall lines. A thorough investigation on these issues is the subject of current work that will be reported in a forthcoming publication. An example of the three-dimensional structure of the outer rainbands simulated by the current model can be found in Franklin (2000).

A zonal-vertical cross section of radar reflectivity, vertical motion, and equivalent potential temperature together with the zonal-vertical (u, w) circulation along line A-B in Fig. 6 is shown in Fig. 7. High radar reflectivity in the eyewall tilts outward with height (Fig. 7a). A relatively sharp vertical gradient at about 500 hPa is visible and results from melting of graupel and snow (Liu et al. 1997). The eye is nearly free of precipitation. Outside the eyewall in the middle and upper troposphere there are regions of stratiform precipitation. Further outside the eyewall, there are several vertically aligned convective cloud features that are associated with the outer rainbands as seen in Fig. 6. As found by Lord et al. (1984) and Liu et al. (1997), our results also show the importance of including the mixed/ice-phase cloud microphysics in producing more realistic cloud structures in model tropical cyclones. In addition, we found that the mixed/ice-phase cloud microphysics played a role in limiting the maximum intensity of the model tropical cyclone, compared with the warm-rain cloud microphysics scheme. This is due to the fact that stronger downdrafts generated in the rainbands by melting of snow and graupel in the mixed/ice-phase scheme lower the equivalent potential temperature in the cyclone boundary layer. A detailed comparison and analysis will be shown in Part II.

Vertical motion in the eyewall is quite asymmetric with a strong updraft to the west that tilts outward with height as well (Fig. 7b). The updraft in the eyewall to the east is weak with a maximum at the upper troposphere, which results from depositional heating associated with the growth of cloud ice, snow, and graupel, and thus is less convective. Downdrafts near the outer edge of the eyewall in the middle levels produce a cold and dry pool with relatively low equivalent potential temperature to the west (Figs. 7b,c). A mesoscale downdraft about 90 km to the east just inside a convective rainband also produces a low equivalent potential temperature pool in the subcloud boundary layer. The air with low equivalent potential temperature in the boundary layer may be advected to and entrained into the eyewall (see wind arrows in Fig. 7c), suppressing the eyewall convection. This plays a role in limiting the cyclone intensity (Powell 1990a,b). Another downdraft occurs near the inner edge of the eyewall (Fig. 7b). This is enhanced by the sublimative cooling of snow and graupel detrained from the eyewall, as suggested by Liu et al. (1997) in their simulation of Hurricane Andrew. An interesting feature of the simulated tropical cyclone is the existence of the air mass with low equivalent potential temperature at the low levels in the eye (Fig. 7c). This seems to be consistent with the eye thermodynamics discussed by Willoughby (1998), which proposed that the air above an inversion has remained in the eye since it was first enclosed when the eyewall formed.

In addition to the overall mature structure, it is interesting to look at the evolution of the model tropical cyclone. To elucidate some important aspects of the intensification processes, we show the time series of radar reflectivity at the surface at 6-h intervals up to 54 h of time integration in Fig. 8. Convection is initiated near

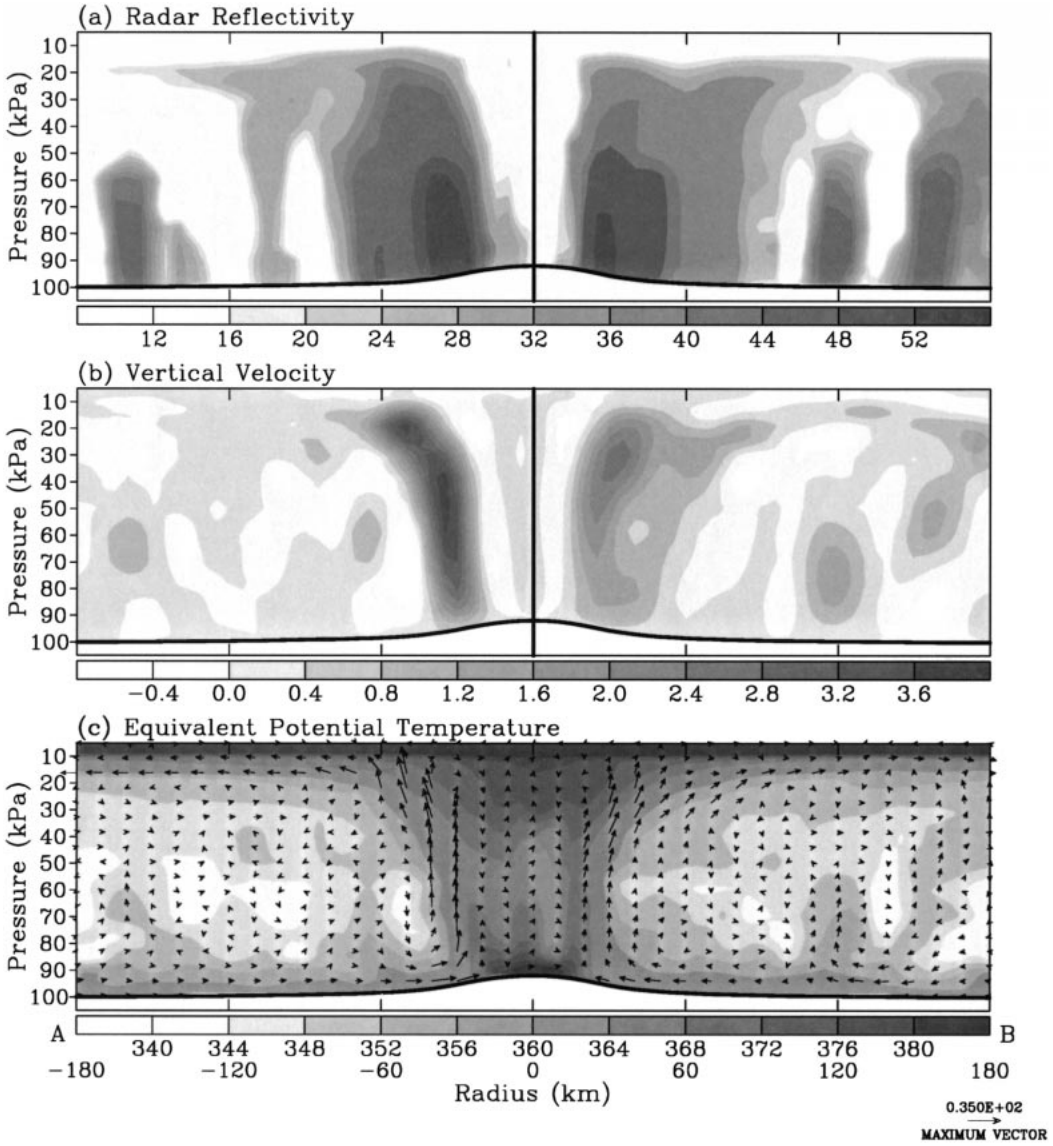

FIG. 7. Vertical cross section of (a) radar reflectivity, (b) vertical velocity, and (c) equivalent potential temperature along line A-B in Fig. 6. Units are dBZ in (a), m s^{-1} in (b), and K in (c). Solid line in each panel shows the surface pressure, and vertical line shows the cyclone center. Arrows in (c) show the zonal-vertical circulation in the same cross section.

the radius of maximum wind where both frictional convergence and evaporation from the ocean are largest (see at 6 h). This convective ring produces a local maximum in potential vorticity in the lower troposphere (not shown), resulting in the development of barotropic instability (Schubert et al. 1999) and thus a breakdown of the convective ring (6–12 h). The broken convective cells partly propagate outward as gravity waves, and partly curve and rotate cyclonically toward the center (12–18 h), and form a nascent eye and an eyewall by 18–24 h. Intensification of the cyclone accompanies the above evolution. This is followed by a steady rapid intensification of the system with the development of a complete eyewall until 54 h from which the cyclone starts its slowly varying evolution (Fig. 4).

As we have already seen from Fig. 7, the model tropical cyclone is typically asymmetric, even within the eyewall region. Similar asymmetric structure has been found in several other tropical cyclone models (Anthes 1972; Tuleya and Kurihara 1975; Kurihara and Bender 1982) in similar model settings (e.g., on an f plane in an environment at rest). Anthes (1972) attributed the development of asymmetric structure, mainly in the upper troposphere, to the dynamical instability in the outflow layer. Tuleya and Kurihara (1975) found that the asymmetric eddies are maintained by energy supply

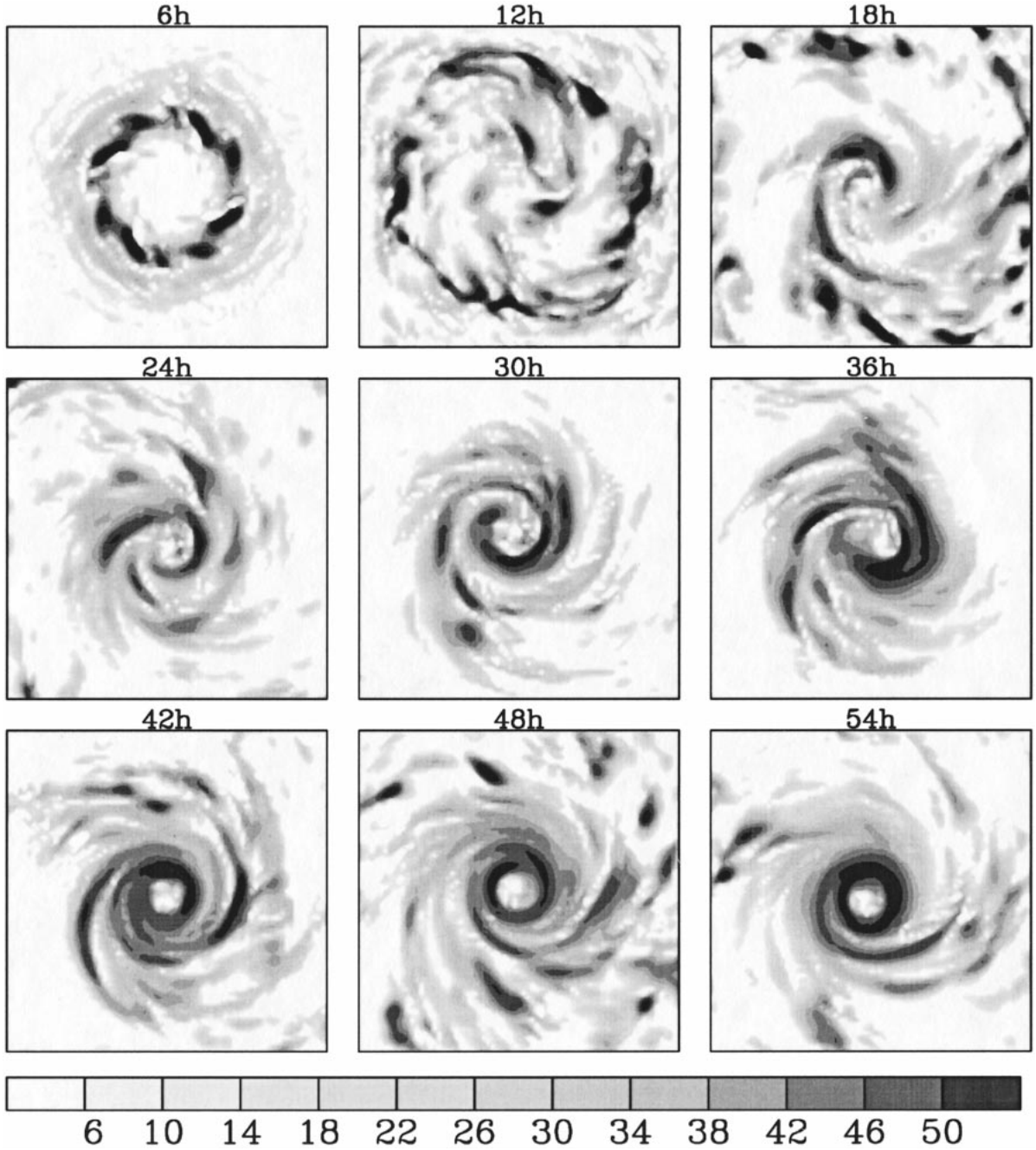

FIG. 8. Model-simulated radar reflectivity (unit: dBZ) at the surface at 6-h intervals up to 54 h in the control experiment. The domain shown in each panel is 400 km by 400 km.

from both azimuthal mean kinetic energy and total potential energy, with the latter being more important during the early development stage. Kurihara and Bender (1982) conducted a high-resolution simulation with the innermost grid spacing of 5 km and found asymmetric structure of the modeled tropical cyclone in various fields. The asymmetric features moved cyclonically within the eyewall at a much longer rotation period than a parcel moving with the mean cyclonic flow within the eyewall. Although these findings have provided evidence of asymmetric structure within the eyewall of model tropical cyclones, the dynamic features and their potential dynamical importance in the tropical cyclone have not been well addressed. Recent studies have paid much more attention to these issues, but most of them have based on the nondivergent barotropic framework (Guinn and Schubert 1993; Montgomery and Kallenbach 1997; Schubert et al. 1999). It is proposed that

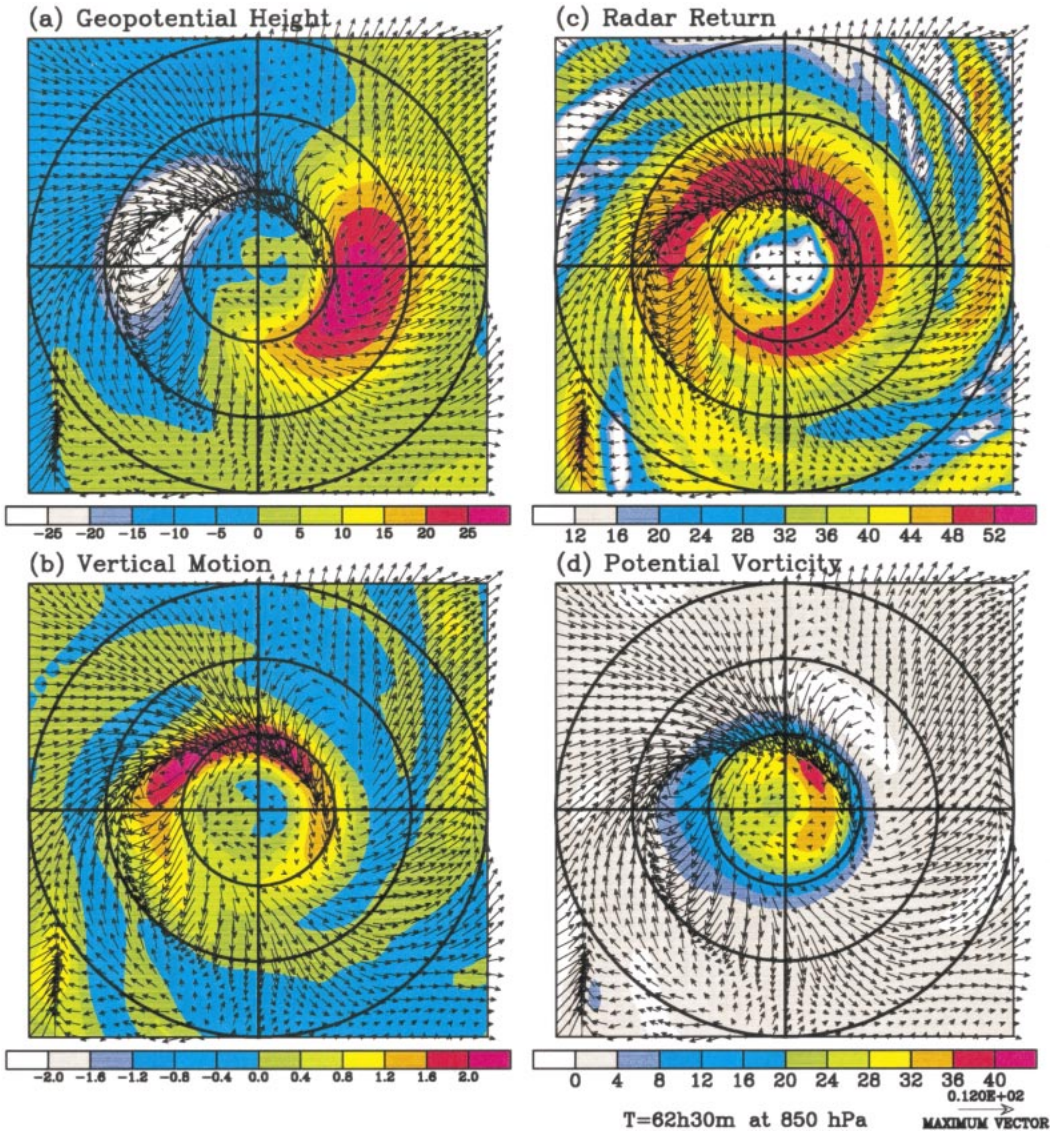

FIG. 9. Shaded in color are fields of the (a) asymmetric geopotential height, (b) total vertical motion, (c) total radar reflectivity, and (d) total potential vorticity, superposed by the asymmetric horizontal winds relative to the moving cyclone, at 850 hPa after 69 h 15 min of time integration. The cross shows the model tropical cyclone center. The circle shows the radius of 30, 60, 90 km from the cyclone center. The domain shown in each panel is 180 km by 180 km.

vortex Rossby waves with low wavenumbers may dominate the asymmetric structure within the tropical cyclone eyewall and may play a role in tropical cyclone structure and intensity changes (Montgomery and Enagonio 1998; Möller and Montgomery 1999). However, in their simulation of Hurricane Andrew with MM5, Liu et al. (1999) found that the asymmetric structure within the eyewall was dominated by the inertial gravity waves. Here, in contrast to Liu et al. (1999), we will provide evidence that vortex Rossby waves are a unique feature within our simulated tropical cyclone core and they may play an important role in the vortex dynamics as already demonstrated in the above-mentioned theoretical studies.

To highlight the dynamical features of the asymmetric structure in the inner core region of the simulated tropical cyclone, we first show in Fig. 9a the asymmetric geopotential height fields and asymmetric horizontal winds relative to the moving cyclone at 850 hPa after 62 h 30 min of time integration. Shown in Figs. 9b–d are the total vertical motion, radar reflectivity, and potential vorticity (PV), respectively, at the same level superposed by the asymmetric wind fields as shown in Fig. 9a. It can be seen that the asymmetric structure in both the geopotential height and horizontal winds is dominated by wavenumber one in the core region within 90-km radius with the maximum amplitude near the radius of maximum wind (Fig. 9a). An interesting fea-

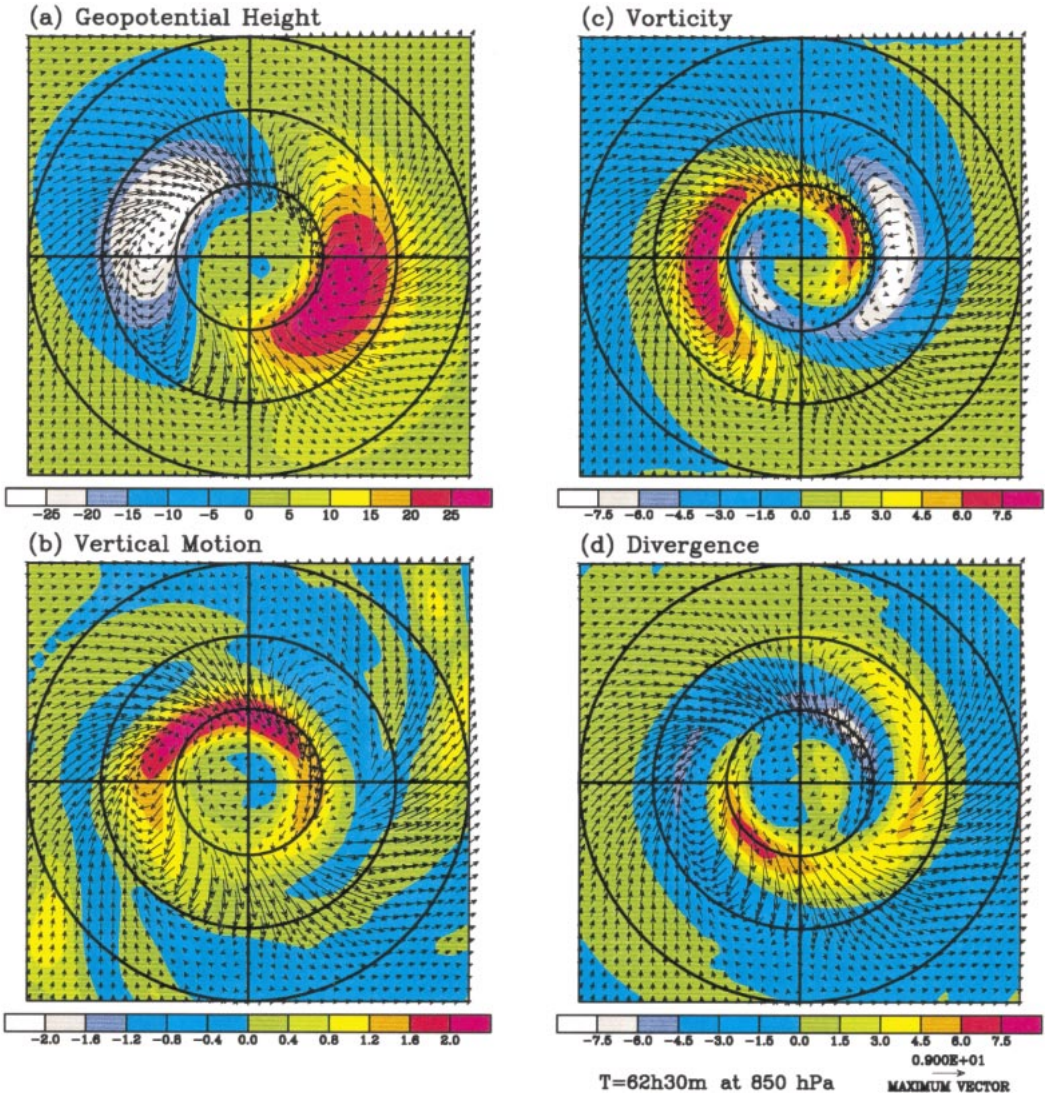

FIG. 10. Shaded in color are fields of the (a) wavenumber-one geopotential height, (b) total vertical motion, (c) wavenumber-one relative vorticity, and (d) wavenumber-one divergence, superposed by the wavenumber-one asymmetric horizontal winds relative to the moving cyclone, at 850 hPa after 69 h 15 min of time integration. The cross shows the model tropical cyclone center. The circle show the radius of 30, 60, 90 km from the cyclone center. The domain shown in each panel is 180 km by 180 km.

ture is that the confluent cyclonic (divergent anticyclonic) circulation associated with the asymmetric winds is collocated with negative (positive) perturbation in the asymmetric geopotential height fields. This indicates that even in the tropical cyclone core region, the motion is quasi-balanced (Shapiro and Montgomery 1993; Montgomery and Lu 1997), although the divergent flow remains large (Fig. 9a). As found for vortex Rossby waves by Montgomery and Lu (1997), the asymmetric wind fields seem to adjust to the height perturbation (Fig. 9a). These features are found to extend from the surface up to about 500 hPa and tilt outward with height (not shown) with outflow (inflow) above the low-level confluent cyclonic (divergent anticyclonic) flow. Such a vertical coupling of the asymmetric structure and the associated asymmetric circulation favor enhanced upward motion to the front (rear) of the low (high) geopotential height perturbation center, but suppressed upward motion to the front (rear) of the high (low) geopotential height perturbation center (Fig. 9b).[1] This results from the strong inflow (outflow) in the lower

[1] Here the front/rear is referred to the direction facing down the azimuthal-mean tangential flow of the model tropical cyclone. Note that this is a Southern Hemisphere tropical cyclone so that cyclonic is clockwise while anticyclonic is counterclockwise. Note also that for clarity, we showed in all figures the vorticity or potential vorticity to be positive for cyclonic but negative for aniticyclonic.

(upper) troposphere in the former region, but outflow (inflow) in the lower (upper) troposphere in the latter region. This strong inflow–outflow couplet also shifts the eyewall a little inward toward the cyclone center in the inflow region (outward in the outflow region), leading to an incomplete polygonal eyewall structure and inner spiral rainbands to the east and southwest (Figs. 9b,c).

Note that the maximum in radar reflectivity occurs to the downwind side of the enhanced updraft region. This downwind displacement is due to the fact that all the hydrometeors in the eyewall clouds are advected cyclonically by the tangential flow of the primary cyclone, while the asymmetric circulation moves at a much slower speed around the cyclone center (see discussion below). The PV fields (Fig. 9d) also show a strong asymmetric structure with a maximum to the northeast within the radius of maximum wind. A low PV region near the cyclone center is surrounded by relatively high PV, and is displaced to the west in the eye region. Further detection indicates that the low PV in the eye in the lower troposphere is a unique feature for our simulated tropical cyclone. Schubert et al. (1999) suggested that such a PV structure satisfies the necessary condition for barotropic instability and may result in the development of small eddies in the eyewall and thus an eyewall breakdown and PV mixing between the eye and the eyewall. We found that the barotropic instability may be one of the candidates that initiate the development of the asymmetric structure in the eyewall. We also found that the asymmetric gyres (or eddies) near the eyewall (Fig. 9a) play a crucial role in initiating the inner spiral rainbands, making the formation of polygonal eyewall and eyewall breakdown (Figs. 9b,c) accompanied by a temporary weakening of the model tropical cyclone (Fig. 4). A full study of these processes and dynamics, including how these asymmetric features are forced and their role in the life cycle of the tropical cyclone is the subject of current work that will be reported in a forthcoming publication.

The wavenumber-one asymmetries in geopotential height, horizontal wind, vorticity, and divergence fields at 850 hPa are shown in Figs. 10a,c,d, respectively. In Fig. 10b, the total vertical motion at the same level is shown again but superposed by the wavenumber-one asymmetric flow. Now we can clearly see that in both the vorticity and divergence fields, the disturbances spiral cyclonically inward with a maximum amplitude near the radius of maximum wind. This structure indicates an outward propogation of the disturbances, similar to the vortex Rossby waves discussed by Montgomery and Kallenbach (1997). Consistent with the finding by Montgomery and Franklin (1998) from an observational assessment, the perturbation vorticity and divergence have similar amplitude even in the cyclone core region. Cyclonic (anticyclonic) vorticity is coupled with convergence (divergence), implying that the disturbances are well coupled with the convective asymmetries in the eyewall. Our vorticity budget shows that convergence-divergence is the main source for vorticity generation, which is nearly balanced by the radial advection of the vorticity of the primary cyclone by the asymmetric flow (not shown). This indicates that any convectively asymmetric forcing in the eyewall can generate low-wavenumber disturbances near the eyewall. The convective asymmetries in the eyewall can be initiated either locally by barotropic instabilities across the eyewall as suggested by Schubert et al. (1999), or remotely by the outer rainbands in the cyclone circulation as indicated by G. Holland (1999, personal communication).

To determine whether the disturbances near the eyewall are vortex Rossby waves, as suggested by Montgomery and Kallenbach (1997), we plot the temporal evolution of the asymmetric vorticity along the eyewall radius (30 km from the cyclone center) from 24 to 120 h of time integration in Fig. 11. As already seen from Fig. 9, the asymmetries near the eyewall are dominated by wavenumber-one structure although wavenumber-two disturbances can be identified frequently but with a smaller amplitude than the wavenumber-one disturbances (Fig. 12). Higher wavenumber disturbances have even smaller amplitudes with no obvious dynamical importance. This is consistent with the results of Smith and Montgomery (1995), who demonstrated that only low wavenumber disturbances can exist near the tropical cyclone core where strong shear damps the high wavenumber disturbances very effectively through the axisymmetrization process. These waves of both wavenumber-one and wavenumber-two move cyclonically along the eyewall with a period of about 113 min at the mature stage. This period is longer during the early development stage due to the weaker azimuthal flow. This period is much longer than that of a parcel moving along the eyewall with the local mean tangential flow of the primary cyclone. The latter is about 50 min in the mature stage (estimated based on 63 m s^{-1} tangential wind), indicating that the waves propagate anticyclonically relative to the tangential flow of the primary cyclone with a phase speed of about 34 m s^{-1}. Although this phase speed is about three times the planetary Rossby waves in the midlatitude atmosphere, it is consistent with the large radial PV gradient near the eyewall in the simulated tropical cyclone (Fig. 9d). Direct comparison of the phase speed of the waves with the theoretical result obtained by Montgomery and Kallenbach (1997) is not straightforward since the assumptions made in deriving the theoretical phase speed cannot be justified from our model results, but in the range estimated for free vortex Rossby waves in the shallow water model by Montgomery and Lu (1997). Meanwhile, quasi-balanced features of the waves as seen from Figs. 9 and 10 imply that the waves (either with wavenumber one or two) are most likely vortex Rossby-type waves (or in general, vorticity waves, PV waves), rather than inertial-gravity waves as those found by Liu et al. (1997). On the other hand, the waves can be identified

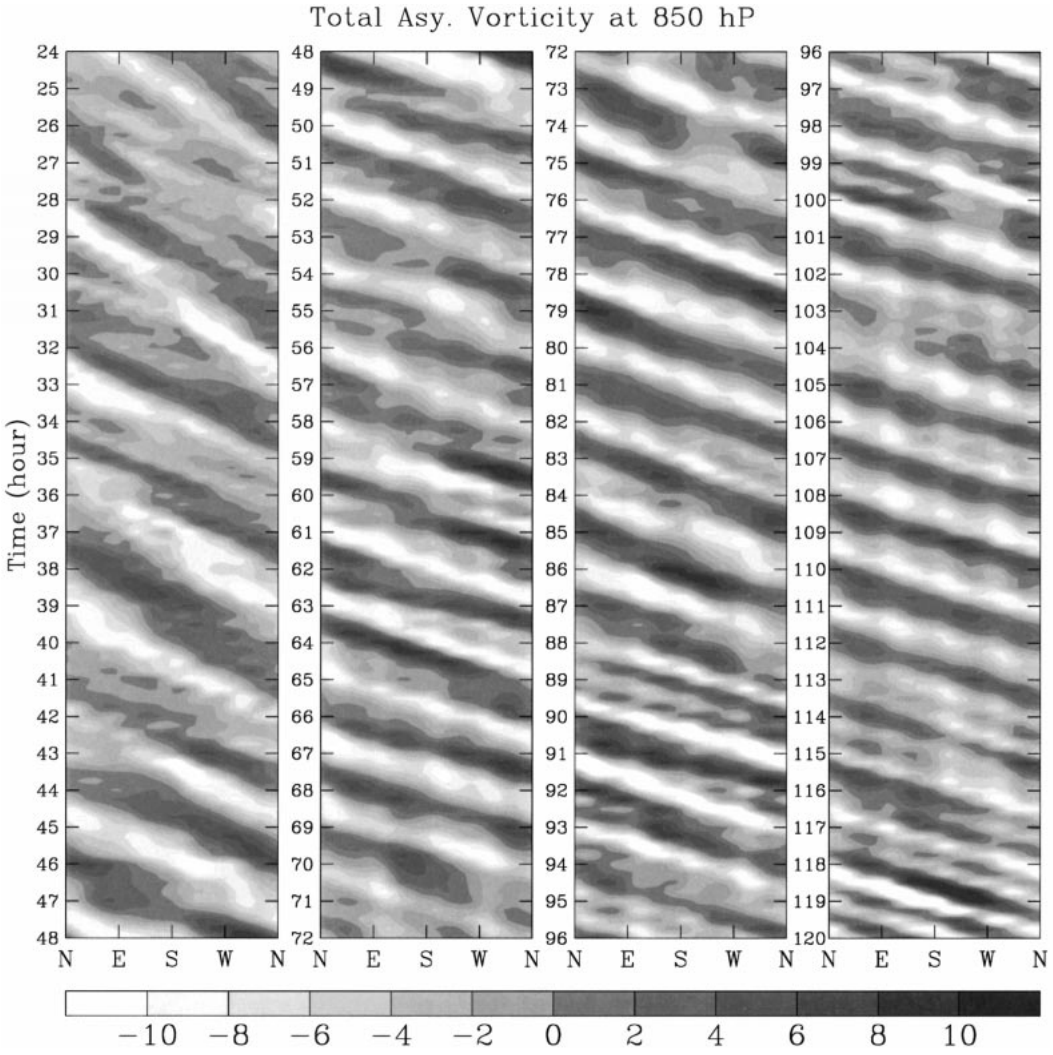

FIG. 11. Azimuthal-time Hovmöller diagram of the asymmetric relative vorticity along a radius of 30 km from the cyclone center at 850 hPa from 24 to 84 h of time integration. This shows a cyclonic rotation of the asymmetric structure (waves) along the eyewall of the simulated tropical cyclone.

only in the near environment of the eyewall where large PV gradients exist, indicating that they are Rossby-type waves since PV gradients are not necessary conditions for the existence of inertial-gravity waves.

Although these vortex Rossby-type waves have largest amplitude near the eyewall, they seem to form just inside the eyewall and then propagate outward (Fig. 13). The PV gradients in our simulated tropical cyclone change sign in the lower troposphere inside of the radius of maximum wind (about 15 km from the cyclone center, Fig. 9d), implying that barotropic instability may be a mechanism for formation of the vortex Rossby waves as suggested by Schubert et al. (1999). Other processes, however, cannot be ruled out, such as the potential role of the asymmetric flow in the upper troposphere (Anthes 1972) and the inward detrainment of hydrometeors from the eyewall in the upper level as indicated above. When the waves propagate outward they can be amplified across the eyewall where convective forcing becomes strongest (about 30–40–km radius, Fig. 13). Further outward, the PV gradients become quite small and the waves lose their identity.

Note that although the propagation of the waves is outward against the inflow of the primary cyclone in the lower troposphere, the wave energy seems to propagate inward from the radius of about 40 km to the cyclone center (Fig. 13). For example, the wave amplitude at 62 h 30 min gets its maximum at a radius of about 40 km, this maximum then shifts consecutively inward for the next wave crests up to 67 h. Similar examples are from 78 to 85 h, 85 to 90 h, and 105 to 110 h. This inward energy propagation is in contrast to the theoretical results by Montgomery and Kallenbach (1997), who found an outward energy dispersion.

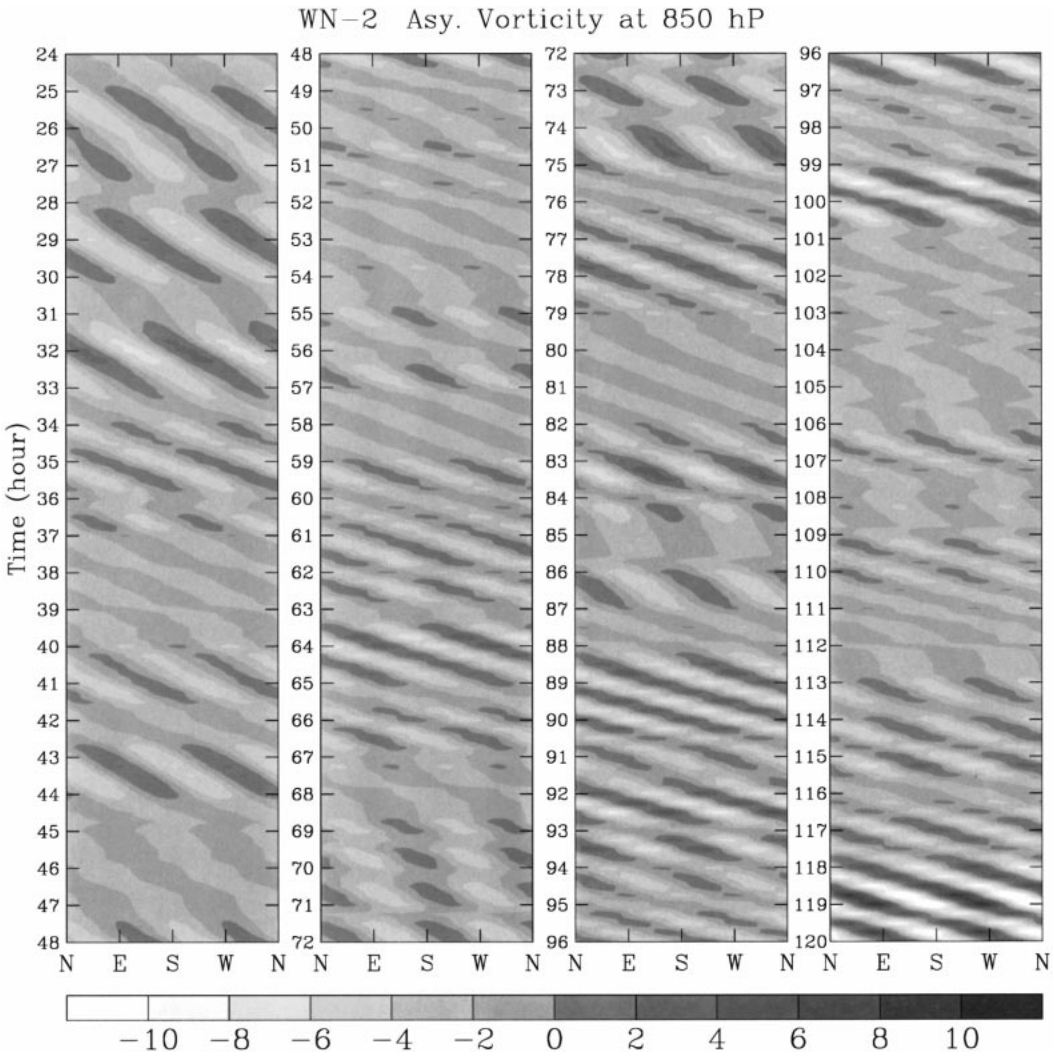

FIG. 12. As in Fig. 11 but for wavenumber-two relative vorticity.

It should be pointed out that in their analytical result, the vorticity of the axisymmetric vortex decreases with radius monotonically, while the PV in our simulated tropical cyclone has a maximum just inside the radius of maximum wind (Fig. 9d). This inversed PV gradient in the eyewall may be responsible for the inward energy dispersion. To give a visible view of this inward energy dispersion, we further plot in Fig. 14 the wavenumber one vorticity at 850 hPa at 30-min intervals from 84 h to 91 h 30 min. We can see that the spiral vorticity waves rotate cyclonically around the cyclone center and propagate outward. If following just one wave crest, one can see that the maximum wave amplitude increases inward with time (from 84 to 87 h, and from 90 to 91 h 30 min), implying an inward energy propagation of the waves and also a vorticity or PV mixing between the eye and the eyewall, as suggested by Schubert et al. (1999). Another interesting feature is that the weakening of the wavenumber-one waves between 87 and 89 h 30 min is accompained by development of wavenumber-two disturbances (Fig. 11), implying that energy transfer between waves with different wavenumbers is possible and worth investigating further. It should be pointed out that although the wavenumber-two disturbances have features similar to the wavenumber-one disturbances discussed above they do not experience a significant outward propagation and are mostly trapped in the eyewall region (not shown).

Another important feature is the rotation of the eyewall with polygonal shape in our simulated tropical cyclone (Fig. 8). We found that the polygonal eyewall rotation results mainly from the cyclonic rotation of the vortex Rossby waves along the eyewall. This supports the recent theoretical study by Kuo et al. (1999), who attribute the eye rotation of Typhoon Herb (1996) to the vorticity waves that propagate around the eyewall. Typhoon Herb had a similar intensity as our sim-

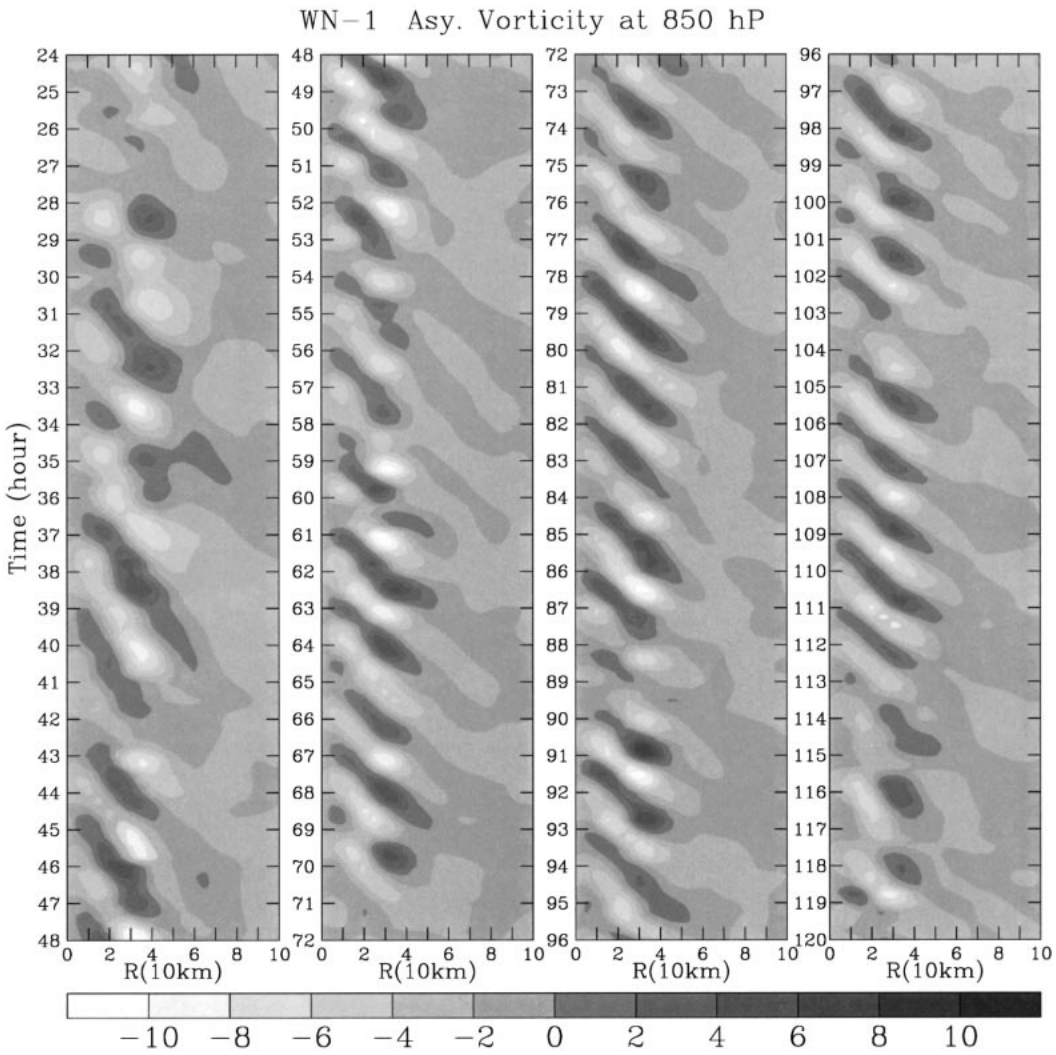

FIG. 13. Radial-time Hovmöller diagram of the wavenumber-one asymmetric relative vorticity from the cyclone center to 100 km to the east at 850 hPa from 24 to 84 h of time integration. This shows an outward propagation of the wavenumber-one vortex Rossby waves in the simulated tropical cyclone.

ulated tropical cyclone and its polygonal eyewall rotated cyclonically with a period of about 144 min (Kuo et al. 1999), very close to the period of the vortex Rossby waves identified from our numerically simulated tropical cyclone although a direct comparison is impossible. Further analyses aimed to address this issue, together with the role of vortex Rossby waves in initiating the inner spiral rainbands and in resulting eyewall breakdown processes in the simulated tropical cyclone, are under way and results will be reported in due course.

5. Conclusions

Although improvements in tropical cyclone track forecasting are quite significant, the skill in prediction of structure and intensity by numerical weather prediction models is still low (e.g., Bender et al. 1993; Kurihara et al. 1995; Kurihara et al. 1998). The latter may be strictly limited by both the use of coarse spatial resolution and the use of unsuitable cumulus convective parameterizations in most operational numerical models. Another key factor limiting the predictability of the tropical cyclone structure and intensity is the uncertainties in the initial conditions, such as the structure, intensity, etc. (Wang 1998). In this sense, the problem of initial conditions remains to be solved even if a high-resolution model is used. Recent efforts in this direction can be referred to Zou and Xiao (2000) and Xiao et al. (2000). There is no doubt that studies with the use of very high-resolution, cloud-resolvable numerical models will contribute to further improvements of current operational numerical models. In this aspect, grid nesting or adaptive grid systems are usually required due

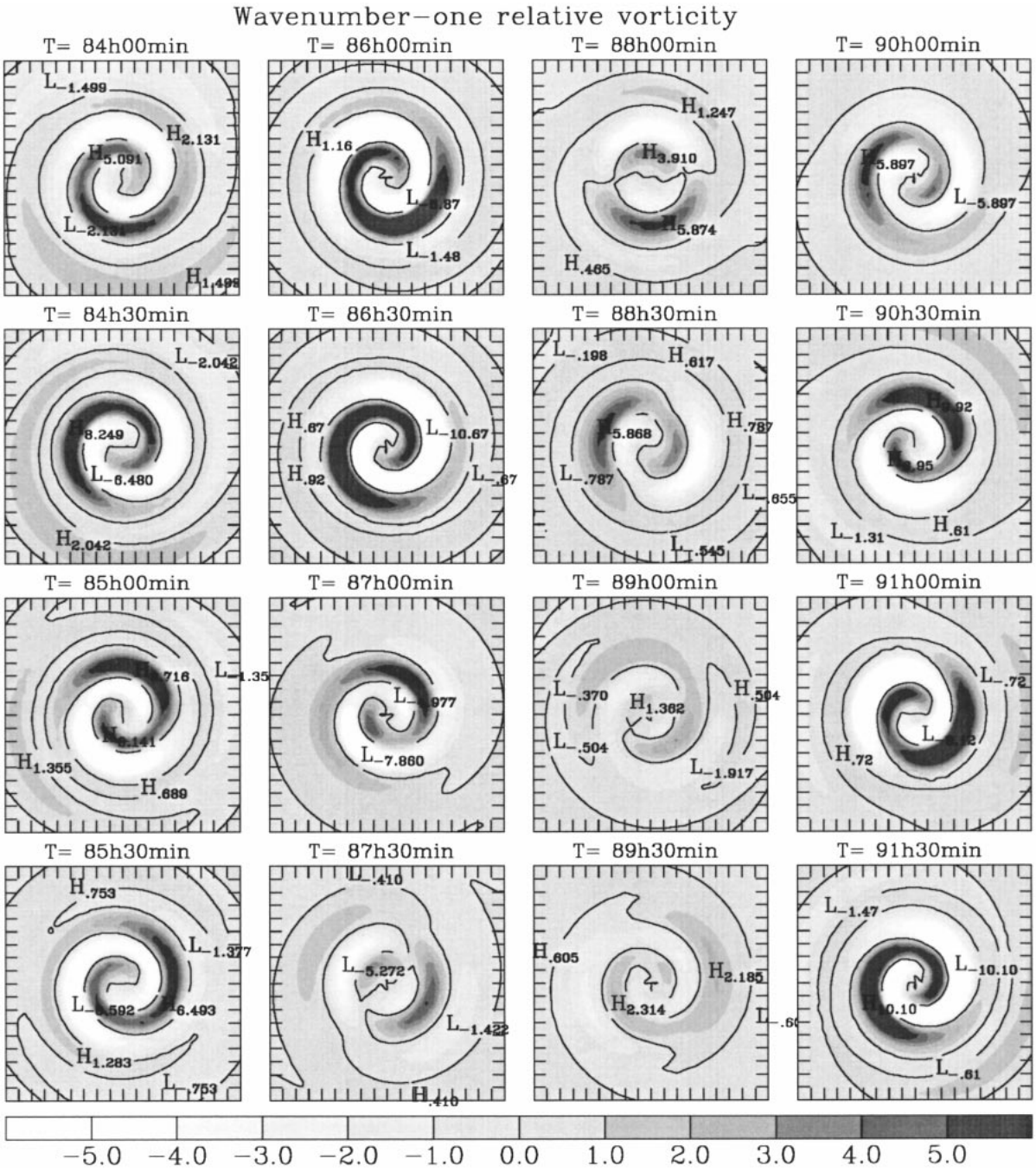

FIG. 14. Wavenumber-one relative vorticity fields at 850 hPa in the cyclone core region at 30 min intervals from 84 to 91 h 30 min, showing the evolution of the wavenumber-one vortex Rossby waves in the simulated tropical cyclone. Contours are those of zero relative vorticity.

to the huge computations associated with explicit cloud microphysics.

A triply nested movable mesh, high-resolution tropical cyclone model with explicit cloud microphysics has been developed and described in detail first in this paper. The model uses hydrostatic primitive equations formulated in Cartesian coordinates in the horizontal and σ coordinates in the vertical. The model consists of 20 layers in the vertical with higher resolution in the planetary boundary layer. A two-way interactive, triply nested movable mesh technique is used so that very high resolution can be achieved in the cyclone core region. The outermost mesh is responsible for representing the evolution of large-scale environmental flow. The inter-

mediate mesh is used to capture the synoptic-scale flow associated with a tropical cyclone so the mesh moves with the model tropical cyclone. The innermost mesh with a grid spacing of 5 km is designed to resolve the central core and spiral rainbands of the tropical cyclone explicitly and moves with the model tropical cyclone as well. An iterative numerical scheme to solve the inverse nonlinear balance equation in σ coordinates in the nested-mesh system is designed for model initialization.

The surface fluxes are calculated based on the Monin-Obkuhov similarity theory with the stability functions being modified for highly unstable conditions as suggested by Fairall et al. (1996). Potential effect of sea spray evaporation by option is included according to the bulk parameterization scheme proposed by Fairall et al. (1994). The turbulent fluxes above the sea surface are calculated based on an E-ϵ turbulence closure scheme, in which both the turbulence kinetic energy and its dissipation rate are prognostic variables (Langland and Liou 1996). To better represent the turbulent mixing in clouds, the buoyancy production term in both the TKE and its dissipation rate equations are modified for in-cloud regions according to Durran and Klemp (1982) and Tripoli (1992). A level-2 turbulence closure scheme is used to initialize the turbulence kinetic energy and its dissipation rate fields.

The cloud microphysics are included based on a bulk parameterization scheme. By this approach, we predict mixing ratios of water vapor, cloud water, rainwater, cloud ice, snow, and graupel. The parameterization of cloud microphysical processes is based on the existing schemes that are extensively tested and used in many other cloud-/mesoscale numerical models in recent years (e.g., Lin et al. 1983; Rutledge and Hobbs 1984; Ikawa and Saito 1991; Krueger et al. 1995; Reisner et al. 1998). A modification was made to the formula for the timescale that determines the rate at which cloud ice converts to snow via the Bergeron process. In the new formula, this timescale is not only a function of temperature as used in earlier applications but also depends on the ice supersaturation and the difference between the saturation mixing ratios on water and ice surfaces.

Two experiments were constructed, with one used to test the movable nested-mesh system and conservative property of the numerical scheme, and the other to demonstrate the capability of the model in simulating the multiscale interactions in tropical cyclones. The results show that the model can be used as a powerful tool for simulating and investigating mesoscale aspects of tropical cyclones, including the genesis, intensification, motion, and complex interactions between a tropical cyclone and its larger-scale environment. Further developments of the model include considering the nonhydrostatic effect, long- and shortwave radiation, land surface processes, and coupling with an ocean model, such as the one that was used in Wang et al. (1997).

Results from a control experiment were discussed in detail. Not only the overall structure and development of the model tropical cyclone are presented but also the asymmetric structure in the cyclone core region is analyzed. The vortex Rossby waves in the simulated tropical cyclone core are identified. These waves are found to be dominated by low wavenumber (one/two) structure, tilt outward with height, and posses quasi-balanced dynamical features in the lower troposphere. They move cyclonically along the eyewall with a ''backward'' phase speed relative to the advective flow near the eyewall, resembling the planetary Rossby waves in the troposphere. They also propagate outward against the inflow of the primary cyclone in the lower troposphere but have an inward energy propagation. This latter feature may favor a mixing of potential vorticity between the eye and the eyewall, as suggested by Schubert et al. (1999). The evolution of these waves is found to play a crucial role in initiating the inner spiral rainbands, causing polygonal eyewall structure and its cyclonic rotation, even resulting in an eyewall breakdown accompanied by an intensity change. Although these processes have been inferred from simple barotropic dynamics and simple baroclinic models in recent years (Guinn and Schubert 1993; Montgomery and Kallenbach 1997; Montgomery and Enagonio 1998; Möller and Montgomery 1999; Schubert et al. 1999; Kuo et al. 1999), the detailed mechanisms for formation of vortex Rossby waves and the manner in which they interact with the eyewall convection and their potential role in causing both structure and intensity changes of tropical cyclones are not well understood. Studies of these processes are the subject of our current work that will be reported in a forthcoming publication.

Acknowledgments. The author is grateful to Drs. Greg Holland and Gary Barnes for carefully reading an earlier version of the manuscript and for helpful comments. Thanks are also due to Jeff Kepert, Noel Davidson, and Sajal Kar for enjoyable discussions, and to two anonymous reviewers for their constructive comments. Part of this study has been supported by the U.S. Office of Naval Research under Grant ONR-00014-94-1-0493. Additional support has been provided by the Frontier Research System for Global Change through the International Pacific Research Center in the School of Ocean and Earth Science and Technology at the University of Hawaii.

APPENDIX A

List of Symbols and Their Meanings

Notation	Description	Value	Unit
a_1	Parameter in Bergeron process		$kg^{1-a_2}\ s^{-1}$
a_2	Parameter in Bergeron process		
C_p	Specific heat of dry air at constant pressure	1004.6	$J\ kg^{-1}\ K^{-1}$
C_{pm}	Specific heat of moist air at constant pressure		$J\ kg^{-1}\ K^{-1}$
d	Grid spacing in horizontal		m
D	Deformation of horizontal wind		s^{-1}
D_u, D_v, D_T, D_q	Horizontal diffusion of momentum, heat, and moisture		$m\ s^{-2}$
D_x	Diameter of a single precipitating particle of species x		m
E	Turbulent kinetic energy (TKE)		$m^2\ s^{-2}$
f	Coriolis acceleration		s^{-1}
F_E	Vertical diffusion of TKE		$m^2\ s^{-3}$
F_q	Vertical diffusion of moisture		$kg\ kg^{-1}\ s^{-1}$
F_T	Vertical diffusion of heat		$K\ s^{-1}$
F_u, F_v	Vertical diffusion of u and v momentums,		$m\ s^{-2}$
F_ε	Vertical diffusion of TKE dissipation rate		$m^2\ s^{-4}$
g	Gravitational acceleration	9.805	$m\ s^{-2}$
G	Source term in the nonlinear balance equation		s^{-2}
H	Sensible heat flux at the sea surface		$W\ m^{-2}$
k	von Kármán constant	0.4	
K	Kinetic energy		$m^2\ s^{-2}$
K_H	Lateral eddy diffusion coefficient	$m^4\ s^{-1}$	
L_v	Latent heat of condensation	$J\ kg^{-1}$	
m_i	Mass of pristine ice crystal	kg	
m_{ir}	Mass of ice crystal with radius r	kg	
m_{ir0}	Mass of ice crystal with radius r_0	kg	
n_i	Number concentration of ice nuclei		m^{-3}
p	Pressure		Pa
p_s	Surface pressure		Pa
q_c	Mixing ratio of cloud water		$kg\ kg^{-1}$
q_g	Mixing ratio of graupel		$kg\ kg^{-1}$
q_i	Mixing ration of cloud ice		$kg\ kg^{-1}$
q_r	Mixing ratio of rainwater		$kg\ kg^{-1}$
q_s	Mixing ratio of snow		$kg\ kg^{-1}$
q_{si}	Saturation mixing ratio for water vapor with respect to ice		$kg\ kg^{-1}$
q_{sw}	Saturation mixing ratio for water vapor with respect to water		$kg\ kg^{-1}$
q_v	Mixing ratio of water vapor		$kg\ kg^{-1}$
Q_l	Latent heat flux due to evaporation of sea spray		$J\ kg^{-1}\ s^{-1}$
Q_m	Rate of diabatic heating		$J\ kg^{-1}\ s^{-1}$
Q_R	Radiative cooling rate		$K\ s^{-1}$
Q_s	Sensible heat flux due to evaporation of sea spray		$J\ kg^{-1}\ s^{-1}$
r	Radius from the vortex center		m
r_m	Radius of initial maximum tangential wind	100.0	km
R	Gas constant for dry air	287.05	$J\ kg^{-1}\ K^{-1}$
S_E	Source term for TKE		$m^2\ s^{-3}$
S_g	Source term for graupel		$kg\ kg^{-1}\ s^{-1}$
S_c	Source term for cloud water		$kg\ kg^{-1}\ s^{-1}$
S_i	Source term for cloud ice		$kg\ kg^{-1}\ s^{-1}$
S_n	Smoothing coefficient for lateral boundaries		
S_r	Source term for rain		$kg\ kg^{-1}\ s^{-1}$
S_s	Source term for snow		$kg\ kg^{-1}\ s^{-1}$
S_v	Source term for water vapor		$kg\ kg^{-1}\ s^{-1}$
S_ε	Source term for TKE dissipation rate		$m^2\ s^{-4}$
t	Time		s
T	Temperature		K
T_v	Virtual temperature		K
u_*	Frictional velocity		$m\ s^{-1}$
u, v	Horizontal components of the wind in the x, y directions		$m\ s^{-1}$
V_m	Maximum tangential wind of the initial vortex	25.0	$m\ s^{-1}$
V_T	Tangential wind of the initial vortex		m s−1
x, y	Horizontal Cartesial coordinates on the f plane or β plane, positive eastward and northward		m m
z	Vertical ordinate, positive upward		m

Notation	Description	Value	Unit
z_u	Roughness length for momentum at the surface		
z_q	Roughness length for moisture at the surface		m
z_T	Roughness length for heat at the surface		m
β	Poleward gradient of the earth vorticity		$m^{-1}\ s^{-1}$
β'	Coefficient for ice depositional growth		
θ	Potential temperture		K
θ_{ref}	Reference potential temperature		K
ε	TKE dissipation rate		$m^2\ s^{-3}$
ρ	Air density		$kg\ m^{-3}$
σ	Vertical coordinate		
$\dot{\sigma}$	Vertical velocity in the σ coordinate		s^{-1}
τ_R	Relaxation time for radiational cooling		s
Φ	Geopotential height		$m^2\ s^{-2}$
ω	Vertical velocity in p coordinates		$Pa\ s^{-1}$
Δt	Time step		s
Δt_1	Timescale needed for an ice crystal to grow from radius r_0 to r		s

APPENDIX B

Initialization Scheme

The model is initialized using an inverse balance equation in σ coordinates described in detail by Wang (1995), but with some modifications. First, the model initial wind fields (u, v) are specified, and then the mass and thermal fields are obtained by solving the inverse balance equation in the σ coordinate system. The nonlinear balance equation takes the following form (Kurihara and Bender 1980; Kurihara et al. 1993; Wang 1995):

$$\nabla^2\Phi + \boldsymbol{\nabla}\cdot(RT\boldsymbol{\nabla}\ \ln p_s) = G, \tag{B1}$$

where G is derived from the momentum distribution and takes the following form on a β plane:

$$G = 2J(u, v) + f\zeta - \beta u, \tag{B2}$$

where β is the meridional gradient of Coriolis parameter f, ζ is the vertical component of relative vorticity, and $J(a, b)$ is the Jacobian operator.

The equations for $\sigma = 1$ and $\sigma < 1$ can be written as

$$\boldsymbol{\nabla}\cdot(RT_s\boldsymbol{\nabla}\ \ln p_s) = G_s - g\nabla^2 z_s, \tag{B3}$$

$$\nabla^2\Phi = \boldsymbol{\nabla}(RT\boldsymbol{\nabla}\ \ln p_s) - G, \tag{B4}$$

where subscript s denotes the surface value and z_s is the elevation of the $\sigma = 1$ surface ($z_s = 0$ in the current version of the model). If the temperature at the surface is given, the surface pressure fields can be obtained by solving (B3) numerically using a relaxation method under the appropriate boundary conditions.

To obtain the initial thermal field, differentiating (B4) with respect to σ and using the hydrostatic relation (6) in dry conditions, we have

$$\nabla^2 T = \boldsymbol{\nabla}\cdot\left(\frac{\partial T}{\partial\ \ln\sigma}\boldsymbol{\nabla}\ \ln p_s\right) - \frac{\partial G}{R\partial\ \ln\sigma}. \tag{B5}$$

To solve (B5), Kurihara and Bender (1980) and Kurihara et al. (1993) replaced T on the rhs by an undisturbed temperature profile. This approximation seems to give large errors for strong disturbances in which the temperature anomalies are large. To improve the accuracy, Wang (1995) proposed a numerical scheme in which the vertical gradient of temperature on the right-hand side of (B5) was approximated by one-sided finite differencing for the temperature anomaly component, and centered differencing for the undisturbed temperature component. Since we use centered differencing in the model, the one-sided differencing used in Wang (1995) is not consistent with the model numerics. Here, we proposed an iterative technique to solve (B5), which can be rewritten as

$$\nabla^2 T^{\nu+1} = \boldsymbol{\nabla}\cdot\left(\frac{\partial T^{\nu}}{\partial\ \ln\sigma}\boldsymbol{\nabla}\ \ln p_s\right) - \frac{\partial G}{R\partial\ \ln\sigma}, \tag{B6}$$

where ν denotes the iteration times. With the undisturbed temperature as the initial guess field for temperature and with a linear interpolation for the temperature between the vertical layers, (B6) can be solved iteratively using a relaxation method. The solution converges very quickly, and three to four iterations are enough to get an accurate numerical solution.

Following Kurihara and Bender (1980), the relaxation proceeds inward from the coarsest to the finest grid resolution. First, the numerical solution is obtained for the coarsest mesh A, under proper lateral boundary conditions, then for B and C, in order, with the boundary condition obtained by interpolation from the coarser mesh. Our numerical results show that the above initialization scheme performs very well and gives balanced initial conditions, with a smooth solution in each domain and across the mesh interfaces as well.

APPENDIX C

A Modified Timescale in the Bergeron Process

The Bergeron process represents the vapor depositional growth of cloud ice or snow at the expense of cloud water in supercooled clouds ($-40°C < T < 0°C$), which is saturated with respect to water and supersaturated with respect to ice due to the difference in saturation vapor pressures of ice and water. The original timescale (Δt_l) that determines the rate at which cloud ice transforms to snow via the Bergeron process can be written as (Koenig 1971)

$$\Delta t_1 = \frac{1}{a_1(1 - a_2)}[m_{ir}^{(1-a_2)} - m_{ir_0}^{(1-a_2)}], \qquad \text{(C1)}$$

where a_1 and a_2 are temperature-dependent parameters (Koenig 1971); m_{ir} and m_{ir0} are the masses of an ice crystal with radius r and r_0 respectively; and the mass (m_i) of an ice crystal is given by

$$m_i = \rho q_i / n_i, \qquad \text{(C2)}$$

where ρ is the air density, q_i the mixing ratio of cloud ice, and n_i the number concentration of cloud ice. Equation (C1) was obtained based on the depositional growth of cloud ice, which was calculated originally by (Koenig 1971)

$$P_{\text{idep}} = a_1(m_i)^{a_2} n_i / \rho, \qquad \text{(C3)}$$

Equation (C3) is only a function of temperature and the ice mixing ratio. Considering the effect of ice supersaturation and the difference between the saturation mixing ratios on water and ice surfaces, (C3) has been modified in many recent applications as (e.g., Ikawa and Saito 1991; Reisner et al. 1998)

$$P_{\text{idep}} = \frac{q_v - q_{si}}{q_{sw} - q_{si}} a_1(m_i)^{a_2} n_i / \rho = \beta' a_1(m_i)^{a_2} n_i / \rho, \qquad \text{(C4)}$$

where $\beta' = (q_v - q_{si})/(q_{sw} - q_{si})$. The corresponding timescale to (C1) then should be modified as

$$\Delta t_1 = \frac{1}{\beta' a_1(1 - a_2)}[m_{ir}^{(1-a_2)} - m_{ir_0}^{(1-a_2)}]. \qquad \text{(C5)}$$

Note that an additional factor $\beta' > 0$ in (C5) compared to (C1) is related to the modification of vapor depositional growth of cloud ice (C4) to the original formulation (C3) used by Koenig (1971) (in that case, $\beta' = 1$).

Lin et al. (1983) used a timescale for an ice crystal to grow from $r_0 = 40$ μm to $r = 50$ μm, which is somewhat artificially set. Based on in situ aircraft observations from Fu and Liou (1993), Krueger et al. (1995) indicated that a more realistic timescale can be defined as the time needed for an ice crystal to grow from 40 to 100 μm. In this case the timescale is much longer than the one used by Lin et al. (1983) and thus the maximum cloud ice content is increased to be about three times larger than that obtained using the original timescale in a column parcel model, and the extent of anvil clouds in increased to more realistic values in a simulation of a tropical squall line. As noted by Krueger et al. (1995), cloud ice continues to be converted to snow by P_{sfi} in the formulation of Lin et al. (1983) and Lord et al. (1984) even when there is no cloud water. Krueger et al. hypothesized that since cloud ice does not fall while snow does in these models, P_{sfi} in this case acts like a crude fall speed parameterization for cloud ice, but the latter is included explicitly in our model.

We argue that there is no reason just to increase the timescale (which originally is only a function of temperature) to reduce the transformation of cloud ice to snow and thus to increase the cloud ice, especially in the region filled with cloud water where the transformation of cloud ice to snow (and cloud water to snow as well) can be very quick. In our new formula (C5), the timescale is not only a function of temperature but depends on the ice supersaturation and the difference between the saturation mixing ratios on water and ice surfaces. Equation (C5) predicts a relatively shorttime scale in regions with cloud water, and a substantially larger timescale in the anvil clouds, outside the regions with cloud water. This is more physically reasonable than the approach proposed by Krueger et al. (1995). A complete evaluation of our new timescale formulation (C5) will be reported separately elsewhere. In our model, r_0 and r are set to be 40 and 60 μm, respectively. Preliminary experiments show that the model results are not sensitive to r in the range of 50–100 μm.

REFERENCES

Anthes, R. A., 1972: The development of asymmetries in a three-dimensional numerical model of the tropical cyclone. *Mon. Wea. Rev.*, **100,** 461–476.

——, 1982: *Tropical Cyclones. Their Evolution, Structure and Effects. Meteor. Monogr.* No. 41, Amer. Meteor. Soc., 208 pp.

Bender, M. A., R. J. Ross, R. E. Tuleya, and Y. Kurihara, 1993: Improvements in tropical cyclone track and intensity forecasts using the GFDL initialization system. *Mon. Wea. Rev.*, **121,** 2046–2061.

Bigg, E. K., 1953: The supercooling of water. *Proc. Phys. Soc. London,* **B66,** 688–694.

Bister, M., and K. A. Emanuel, 1998: Dissipative heating and hurricane intensity. *Meteor. Atmos. Phys.*, **55,** 233–240.

Detering, H. W., and D. Etling, 1985: Application of the E-ϵ turbulence model to the atmospheric boundary layer. *Bound.-Layer Meteor.*, **33,** 113–133.

Dudhia, J., J. Klemp, W. Skamarock, D. Dempsey, Z. Janjic, S. Benjamin, and J. Brown, 1998: A collaborative effort towards a future community mesoscale model (WRF). Preprints, *Twelth Conf. on Numerical Weather Prediction,* Phoenix, AZ, Amer. Meteor. Soc., 242–243.

Durran, D. R., and J. B. Klemp, 1982: On the effects of moisture on the Brunt–Vaisälä frequency. *J. Atmos. Sci.*, **39,** 2152–2158.

Fairall, C. W., J. D. Kepert, and G. J. Holland, 1994: The effect of sea spray on surface energy transports over the ocean. *Global Atmos. Ocean System,* **2,** 121–142.

——, E. F. Bradley, D. P. Rogers, J. B. Edson, and G. S. Young, 1996: Bulk parameterization of air–sea fluxes for Tropical

Ocean-Global Atmosphere Coupled Ocean Atmosphere Response Experiment. *J. Geophys. Res.*, **110**(C2), 3747–3764.
Frank, W. M., 1977: The structure and energetics of the tropical cyclone. I: Storm structure. *Mon. Wea. Rev.,* **105,** 1119–1135.
Franklin, C. N., 2000: Dynamics and energetics of tropical cyclone rainbands. Preprints, *24th Conf. on Hurricanes and Tropical Meteorology*, Fort Lauderdale, FL, Amer. Meteor. Soc., 33–34.
Fu, Q., and K. N. Liou, 1993: Parameterization of the radiative properties of cirrus clouds. *J. Atmos. Sci.,* **50,** 2008–2025.
Garratt, J. R., 1992: *The Atmospheric Boundary Layer*. Cambridge University Press, 316 pp.
Grell, G. A., J. Dudhia, and D. R. Stauffer, 1994: A description of the fifth generation Penn State/NCAR mesoscale model (MM5). NCAR Tech. Note NCAR/TN-398+STR, 122 pp.
Guinn, T., and W. H. Schubert, 1993: Hurricanes spiral bands. *J. Atmos. Sci.,* **50,** 3380–3404.
Hallett, J., and S. C. Mossop, 1974: Production of secondary ice particles during the riming process. *Nature,* **249,** 26–28.
Heymsfield, A. J., and L. J. Donner, 1990: A scheme for parameterizing ice-cloud water content in general circulation models. *J. Atmos. Sci.,* **47,** 1865–1877.
Holland, G. J., 1997: Maximum potential intensity of tropical cyclones. *J. Atmos. Sci.,* **54,** 2519–2541.
Hsie, E. Y., R. D. Farley, and H. D. Orville, 1980: Numerical simulation of ice phase convective cloud seeding. *J. Appl. Meteor.*, **19,** 950–977.
Ikawa, M., and K. Saito, 1991: Description of a nonhydrostatic model developed at the Forecast Research Department of the MRI. Tech. Res. MRI No. 28, Meteorological Research Institute, Japan, 238 pp.
Kessler, E., 1969: *On the Distribution and Continuity of Water Substance in Atmospheric Circulation. Meteor. Monogr.,* No. 10, Amer. Meteor. Soc., 84 pp.
Koenig, L. R., 1971: Numerical modeling of ice deposition. *J. Atmos. Sci.,* **28,** 226–237.
Krueger, S. K., Q. Fu, and K. N. Liou, 1995: Improvements of an ice-phase microphysics parameterization for use in numerical simulations of tropical convection. *J. Appl. Meteor.,* **34,** 281–287.
Kuo, H.-C., R. T. Williams, and J.-H. Chen, 1999: A possible mechanism for the eye rotation of Typhoon Herb. *J. Atmos. Sci.,* **56,** 1659–1673.
Kurihara, Y., and M. A. Bender, 1980: Use of a movable nested mesh model for tracking a small vortex. *Mon. Wea. Rev.,* **108,** 1792–1809.
——, and ——,1982: Structure and analysis of the eye of a numerically simulated tropical cyclone. *J. Meteor. Soc. Japan,* **60,** 381–395.
——, ——, and R. T. Ross, 1993: An initialization scheme of hurricane models by vortex specification. *Mon. Wea. Rev.,* **121,** 2030–2045.
——, ——, R. E. Tuleya, and R. J. Ross, 1995: Improvements in the GFDL hurricane prediction system. *Mon. Wea. Rev.,* **123,** 2791–2801.
——, R. E. Tuleya, and M. A. Bender, 1998: The GFDL hurricane prediction system and its performance in the 1995 hurricane season. *Mon. Wea. Rev.,* **126,** 1306–1322.
Langland, R. H., and C.-S. Liou, 1996: Implementation of an E-ϵ parameterization of vertical subgrid-scale mixing in a regional model. *Mon. Wea. Rev.*, **124,** 905–918.
Large, W. G., and S. Pond, 1982: Sensible and latent heat flux measurements over the ocean. *J. Phys. Oceanogr.,* **12,** 464–482.
Lilly, D. K., 1964: Numerical solutions for the shape-preserving two-dimensional thermal convection element. *J. Atmos. Sci.,* **21,** 83–98.
Lin, Y.-L., R. D. Farley, and H. D. Orville, 1983: Bulk parameterization of the snow field in a cloud model. *J. Climate Appl. Meteor.,* **22,** 1065–1092.
Liu, Y., D.-L. Zhang, and M. K. Yau, 1997: A multiscale numerical study of Hurricane Andrew (1992). Part I: Explicit simulation and verification. *Mon. Wea. Rev.,* **125,** 3073–3093.
——, ——, and ——,1999: A multiscale numerical study of Hurricane Andrew (1992). Part II: Kinematics and inner-core structure. *Mon. Wea. Rev.,* **127,** 2597–2616.
Lord, S. J., H. E. Willoughby, and J. M. Piotrowicz, 1984: Role of a parameterized ice-phase microphysics in an axisymmetric, nonhydrostatic tropical cyclone model. *J. Atmos. Sci.,* **41,** 2836–2848.
McCumber, M., W.-K. Tao, and J. Simpson, 1991: Comparison of ice-phase microphysical parameterization schemes using numerical simulation of tropical convection. *J. Appl. Meteor.,* **30,** 985–1004.
Molinari, J., and M. Dudeck, 1992: Parameterization of convective precipitation in mesoscale numerical models: A critical review. *Mon. Wea. Rev.,* **120,** 326–344.
Möller, J. D., and M. T. Montgomery, 1999: Vortex Rossby waves and hurricane intensification in a barotropic model. *J. Atmos. Sci.,* **56,** 1674–1687.
Montgomery, M. T., and R. J. Kallenbach, 1997: A theory for vortex Rossby-waves and its application to spiral bands and intensity changes in hurricanes. *Quart. J. Roy. Meteor. Soc.,* **123,** 435–465.
——, and C. Lu, 1997: Free waves on barotropic vortices. Part I: Eigenmode Structure. *J. Atmos. Sci.,* **54,** 1868–1885.
——, and J. Enagonio, 1998: Tropical cyclogenesis via convectively forced vortex Rossby waves in a three-dimensional quasigeostrophic model. *J. Atmos. Sci.,* **55,** 3176–3207.
——, and J. L. Franklin, 1998: An assessment of the balance approximation in hurricanes. *J. Atmos. Sci.,* **55,** 2193–2200.
Ooyama, K. V., 1982: Conceptual evolution of the theory and modeling of the tropical cyclone. *J. Meteor. Soc. Japan,* **60,** 369–379.
Orville, H. D., and F. I. Kopp, 1977: Numerical simulation of the life history of a hailstorm. *J. Atmos. Sci.,* **34,** 1596–1618.
Powell, M. D., 1990a: Boundary layer structure and dynamics in outer hurricane rainbands. Part I: Mesoscale rainfall and kinematic structure. *Mon. Wea. Rev.,* **118,** 891–917.
——, 1990b: Boundary layer structure and dynamics in outer hurricane rainbands. Part II: Downdraft modification and mixed layer recovery. *Mon. Wea. Rev.,* **118,** 919–938.
Purser, R. J., and L. M. Leslie, 1988: A semi-implicit, semi-Lagrangian finite-difference scheme using high-order spatial differencing on a nonstaggered grid. *Mon. Wea. Rev.,* **116,** 2069–2080.
Reisner, J., R. M. Rasmussen, and R. T. Bruintjes, 1998: Explicit forecasting of supercooled liquid water in winter storms using the MM5 mesoscale model. *Quart. J. Roy. Meteor. Soc.,* **124,** 1071–1107.
Rosenthal, S. L., 1978: Numerical simulation of tropical cyclone development with latent heat release by the resolvable scales. I: Model description and preliminary results. *J. Atmos. Sci.,* **35,** 258–271.
Rotunno, R., and K. A. Emanuel, 1987: An air–sea interaction theory for typical cyclones. Part II: Evolutionary study using a nonhydrostatic axisymmetric numerical model. *J. Atmos. Sci.,* **44,** 542–561.
Rutledge, S. A., and P. V. Hobbs, 1983: The mesoscale and microscale structure and organization of clouds and precipitation in midlatitude cyclones. VIII: A model for the ''seeder-feeder'' process in warm-frontal rainbands. *J. Atmos. Sci.,* **40,** 1185–1206.
——, and ——, 1984: The mesoscale and microscale structure and organization of clouds and precipitation in midlatitude cyclones. XII: A diagnostic modeling study of precipitation development in narrow cloud-frontal rainbands. *J. Atmos. Sci.,* **41,** 2949–2972.
Schubert, W. H., M. T. Montgomery, R. K. Taft, T. A. Guinn, S. R. Fulton, J. P. Kossin, and J. P. Edwards, 1999: Polygonal eyewall, asymmetric eye contraction and potential vorticity mixing in hurricanes. *J. Atmos. Sci.,* **56,** 1197–1223.
Shapiro, L. J., and M. T. Montgomery, 1993: A three-dimensional

balance theory for rapidly rotating vortices. *J. Atmos. Sci.*, **50,** 3322–3335.
Smith, G. B., and M. T. Montgomery, 1995: Vortex axisymmetrization: Dependence on azimuthal wavenumber or asymmetric radial structure changes. *Quart. J. Roy. Meteor. Soc.*, **121,** 1615–1650.
Tripoli, G. J., 1992: An explicit three-dimensional nonhydrostatic numerical simulation of a tropical cyclone. *Meteor. Atmos. Sci.*, **49,** 229–254.
Tuleya, R. E., and Y. Kurihara, 1975: The energy and angular momentum budgets of a three-dimensional tropical cyclone model. *J. Atmos. Sci.*, **32,** 287–301.
Wang, Y., 1995: An inverse balance equation in sigma-coordinates for model initializations. *Mon. Wea. Rev.*, **123,** 482–488.
——, 1998: On the bogusing of tropical cyclones in numerical models: The influence of vertical structure. *Meteor. Atmos. Phys.*, **65,** 153–170.
——, 1999: A triply-nested movable mesh tropical cyclone model with explicit cloud microphysics. BMRC Research Report 74, Bureau of Meteorology Research Center, 81 pp.
——, B. Wang, G. J. Holland, and L. Wu, 1997: Ocean response to a moving tropical cyclone in a coupled ocean–tropical cyclone boundary layer model. Preprints, *22d Conf. on Hurricanes and Tropical Meteorology*, Fort Collins, CO, Amer. Meteor. Soc., 86–87.
——, J. D. Kepert, and G. J. Holland, 1999: The impact of sea spray evaporation on tropical cyclone intensification. Preprints, *23d Conf. on Hurricanes and Tropical Meteorology*, Dallas, TX, Amer. Meteor. Soc., 26–29.
Willoughby, H. E., 1988: The dynamics of tropical cyclone core. *Aust. Meteor. Mag.*, **36,** 183–191.
——, 1998: Tropical cyclone eye thermodynamics. *Mon. Wea. Rev.*, **126,** 3053–3067.
——, H.-L. Jin, S. J. Lord, and J. M. Piotrowicz, 1984: Hurricane structure and evolution as simulated by an axisymmetric, nonhydrostatic numerical model. *J. Atmos. Sci.*, **41,** 1169–1186.
Wu, J., 1982: Wind-stress coefficients over sea surface from breeze to hurricane. *J. Geophys. Res.*, **87,** 9704–9706.
Xiao, Q., X. Zou, and B. Wang, 2000: Initialization and simulation of a landfalling hurricane using a variational bogus data assimilation scheme. *Mon. Wea. Rev.*, **128,** 2252–2269.
Yamasaki, M., 1977: A preliminary experiment of tropical cyclone without parameterizing the effects of cumulus convection. *J. Meteor. Soc. Japan*, **55,** 11–30.
Zhang, D.-L., and E. Altshuler, 1999: The effects of dissipative heating on hurricane intensity. *Mon. Wea. Rev.*, **127,** 3032–3038.
——, H.-R. Chang, N. L. Seaman, T. T. Warner, and J. M. Fritsch, 1986: A two-way interactive nesting procedure with variable terrain resolution. *Mon. Wea. Rev.*, **114,** 1330–1339.
Zou, X., and Q. Xiao, 2000: Studies on the initialization and simulation of a mature hurricane using a variational bogus data assimilation scheme. *J. Atmos. Sci.*, **57,** 836–860.